

**UNIVERSITY OF SÃO PAULO
SÃO CARLOS SCHOOL OF ENGINEERING**

MAIARA FERNANDA MORENO

**In-situ Study of Residual Stress Evolution in Zr(C,N)/ α -Al₂O₃ and Zr(C,N)/k-
Al₂O₃ CVD Multilayers during Thermal Cycling**

**Estudo In-situ da Evolução de Tensões Residuais em Multicamadas de CVD em
Zr(C,N)/ α -Al₂O₃ e Zr(C,N)/k-Al₂O₃ durante Ciclos Térmicos**

**São Carlos
2019**

MAIARA FERNANDA MORENO

In-situ Study of Residual Stress Evolution in Zr(C,N)/ α -Al₂O₃ and Zr(C,N)/k-Al₂O₃ CVD Multilayers during Thermal Cycling

Estudo In-situ da Evolução de Tensões Residuais em Multicamadas de CVD em Zr(C,N)/ α -Al₂O₃ e Zr(C,N)/k-Al₂O₃ durante Ciclos Térmicos

Corrected Version

Dissertation presented to the Post-Graduate Program in Materials Science and Engineering of the University of São Paulo, to obtain the title of Master's Degree in Sciences.

Concentration area: Development, Characterization and Application of Materials

Supervisor: Haroldo Cavalcanti Pinto

**São Carlos
2019**

I AUTHORIZE TOTAL OR PARTIAL REPRODUCTION OF THIS WORK BY ANY CONVENTIONAL OR ELECTRONIC MEANS, FOR RESEARCH PURPOSES, SO LONG AS THE SOURCE IS CITED.

Ficha catalográfica preparada pela Seção de Tratamento da Informação do Serviço de Biblioteca – EESC/USP

MORENO, Maiara Fernanda.
M843i In-situ study of residual stress evolution in Zr(C,N)/ α -Al₂O₃ and Zr(C,N)/k-Al₂O₃ CVD multilayers during thermal cycling /Maiara Fernanda Moreno ; supervisor Haroldo Cavalcanti Pinto. São Carlos, 2019.

Dissertation (Master - Pos-graduate program in Materials Science and Engineering Concentration area development, characterization and application of materials)-- São Carlos School of Engineering of University of São Paulo, 2019.

1. Residual stress. 2. Thin films. 3. In-situ X-ray diffraction.
4. Thermal cycling. 5. CVD. 6. Composite design. I. Title

ACKNOWLEDGEMENTS

I would like to thank Assoc. Prof. Dr. Haroldo Cavalcanti Pinto for accept me in his research group since 2016, his dedication and for sharing his knowledge with me.

Thanks to Sandvik Coromant R&D in Stockholm, for providing the necessary samples for the development of this research.

Dr. Manuela Klaus and Dr. Christoph Genzel from the Helmholtz-Zentrum Berlin (HZB) are acknowledged for the energy-dispersive X-ray diffraction measurements using synchrotron radiation.

I thank the São Carlos School of Engineering, for the opportunity of accomplishment of the master's course.

Thanks to São Paulo Research Foundation (FAPESP), grant #2017/14386-9, for granting the master's degree and for the financial support to carry out this research.

Thanks to Bruna Callegari, PhD student, for her help during LNLS experiments.

I would like to express my special thanks to Priv.-Doz. Dr. techn. José Luis García of Sandvik Coromant R&D. Thank you so much for giving me his time, knowledge, experience, patience and for his support and true friendship.

Finally, I thank my parents for the love and the support, without you, I would not have come so far.

In this work, all synchrotron measurements were carried out by prof. Genzel and his working group at EDDI station in HZB-Berlin. The sample production and metallographic investigations were done by Jeanette Persson and Raluca Morjan Brenning at Sandvik Coromant R&D.

I participated on the design of the experiments, carried out the interpretation of the synchrotron measurements results, the plotting of all graphics, as well as the discussions and conclusions presented in this chapter.

FOLHA DE JULGAMENTO

Candidata: Engenheira **MAIARA FERNANDA MORENO**.

Título da dissertação: "Estudo *in-situ* da evolução de tensões residuais em multicamadas de CVD em Zr(C,N)/ α -Al₂O₃ e Zr(C,N)/k-Al₂O₃ durante ciclos térmicos".

Data da defesa: 13/08/2019.

Comissão Julgadora:

Resultado:

Prof. Associado **Haroldo Cavalcanti Pinto**
(Orientador)
(Escola de Engenharia de São Carlos/EESC)

APROVADO

Prof. Dr. **José Luis García**
(AB Sandvik Coromant R&D)

APROVADO

Prof. Dr. **Rodrigo Santiago Coelho**
(Serviço Nacional de Aprendizagem Industrial/SENAI)

APROVADO

Coordenador do Programa de Pós-Graduação em Ciências e Engenharia de Materiais:
Prof. Associado **Rafael Salomão**

Presidente da Comissão de Pós-Graduação:
Prof. Titular **Murilo Araujo Romero**

RESUMO

MORENO, M.F. **Estudo In-situ da Evolução de Tensões Residuais em Multicamadas de CVD em $Zr(C,N)/\alpha-Al_2O_3$ e $Zr(C,N)/\kappa-Al_2O_3$ durante Ciclos Térmicos**. 74p. Dissertação (Mestrado) – Escola de Engenharia de São Carlos, Universidade de São Paulo, São Carlos, 2019.

O presente trabalho trata da análise de tensões residuais de filmes finos em ferramentas de corte revestidas utilizadas em aplicações de fresamento. Uma limitação de desgaste típica é a formação de trincas na forma de “pente”, que levam ao lascamento e falha das ferramentas. A resistência às trincas depende da capacidade das ferramentas revestidas de reduzir a formação destas, que são originadas no revestimento e se propagam para dentro do carbetto. Ajustando a condição de tensão residual do revestimento/carbetto cementado (que depende, entre outros, do CTE das camadas, o método de processamento, o pré ou pós-tratamento) a resistência à falha pode ser melhorada. O sistema $Ti(C,N)/\alpha-Al_2O_3$ é o mais utilizado na indústria. Recentemente, um revestimento alternativo com resistência melhorada a estas trincas baseado em $Zr(C,N)/\alpha-Al_2O_3$ foi desenvolvido. Em algumas aplicações, o uso de $\kappa-Al_2O_3$ é vantajoso. Neste trabalho, as análises de tensões residuais de revestimentos de $Zr(C,N)/\kappa-Al_2O_3$ e $Zr(C,N)/\alpha-Al_2O_3$ produzidos por (CVD) foram realizadas utilizando difração de raios X por dispersão de energia. As tensões residuais foram analisadas “in situ” nas condições de temperatura do ciclo variando de RT a 800°C, a fim de verificar a influência dos diferentes sistemas na evolução e no comportamento dos tensões residuais dos compósitos. Além disso, a influência do microjateamento na tensão residual dos filmes finos foi investigada. Observou-se que ambos os sistemas $Zr(C,N)/\kappa-Al_2O_3$ e $Zr(C,N)/\alpha-Al_2O_3$ apresentam comportamento cíclico semelhante de tensão residual. O efeito do processo de jateamento está confinado à camada $\alpha-Al_2O_3$, que desenvolve altas tensões residuais de compressão. Os resultados deste trabalho fornecem informações valiosas para o projeto de novos sistemas de revestimento com maior resistência às trincas.

Palavras-chave: Tensão residual; Filmes finos; In-situ Difração de raios X; Ciclo térmico; CVD; Design de compósitos

ABSTRACT

MORENO, M. F. **In-situ Study of Residual Stress Evolution in Zr(C,N)/ α -Al₂O₃ and Zr(C,N)/ κ -Al₂O₃ CVD Multilayers during Thermal Cycling** 2019. 74p. Dissertation (Master) – São Carlos School of Engineering, University of São Paulo, São Carlos, 2019.

The present work analyses the residual stresses of thin films in coated cutting tools used in milling applications. Typical wear limitation is the formation of comb cracks, which lead to chipping and failure of the tools. The resistance to comb cracks depends on the ability of the coated tools to reduce the formation of thermo-mechanical cracks, which are originated in the coating and propagate into the carbide. By adjusting the residual stress condition of the coating/carbide substrate (which depends among others on the coefficient of thermal expansion of the layers, the processing method as well as the pre-or post-treatment) the resistance to comb crack failure can be improved. The Ti(C,N)/ α -Al₂O₃ system is the most common used in the industry. Recently, an alternative coating with improved comb crack resistance based on Zr(C,N)/ α -Al₂O₃ has been developed. In some applications the use of κ -Al₂O₃ is of advantage. In this work the residual stress analyses of Zr(C,N)/ κ -Al₂O₃ and Zr(C,N)/ α -Al₂O₃ coatings produced by (CVD) were carried out using Energy Dispersive X-ray diffraction. Furthermore, the residual stresses were analyzed “in situ” at cycling temperature conditions ranging from RT to 800°C in order to verify the influence of the different systems on the residual stress evolution and behaviour of the composites. In addition, the influence of micro-top-blasting on the residual stress of the thin films was investigated. It was observed that both the Zr(C,N)/ κ -Al₂O₃ and Zr(C,N)/ α -Al₂O₃ systems present similar residual stress cycling behaviour. The effect of the top-blasting process is confined to the α -Al₂O₃ layer, which develops high compressive residual stresses. The results of this work provides valuable information for the design of novel coating systems with enhanced resistance to comb cracks.

Keywords: Residual stress; Thin films; In-situ X-ray diffraction; Thermal cycling; CVD; Composite design

LIST OF FIGURES

Figure 1 – Comb cracks in milling inserts	17
Figure 2 – SEM image of a cemented carbide	21
Figure 3 – CVD line	22
Figure 4 – The principle of Bragg reflection.....	26
Figure 5 – Definition of the sample reference system (S) and the laboratory system (L) in X-Ray analysis. (φ, ψ) denote the azimuth and inclination angle, respectively, of the measuring direction L_3 with respect to S	27
Figure 6 – Schematic view of X-ray diffractometer	28
Figure 7 – The principle of the $\sin^2\psi$ method for the analysis of residual stress.....	31
Figure 8 – Different blasting particle types and effects on surface materials.....	33
Figure 9 – Cutting tool used in the milling	34
Figure 10 – Comb crack-principal and lateral crack	36
Figure 11 – Insert for the stress analyses	38
Figure 12 – Schematic view of the components of EDDI beamline	39
Figure 13 – Diffraction elastic constants of a) Al_2O_3 and b) ZrN calculated by the models of Voigt, Reuss and Eshelby-Kröner.....	41
Figure 14 – SEM images for Zr(C,N)-based system.....	43
Figure 15 – Diffractogram for a Zr(C,N)-based system	45
Figure 16 – Integral line intensity for Al_2O_3 layer	47
Figure 17 – Integral line intensity for Zr(C,N) layer.....	48
Figure 18 – d^{hkl} vs. $\sin^2\psi$ curves for the Zr(C,N)_k sample of $\kappa-Al_2O_3$ layer for the 022 and 122 hkl planes	49
Figure 19 – d^{hkl} vs. $\sin^2\psi$ curves for the Zr(C,N)_k sample of Zr(C,N) layer for the 111 and 222 hkl planes	50
Figura 20 – Example of data obtained of residual stresses for different (hkl) planes, i.e different depths within the sub-layers	52
Figura 21 – Residual stresses for the sample Zr(C,N)_ α	53
Figura 22 – Residual stresses for the sample Zr(C,N)_ α _b.....	54
Figura 23 – Residual stresses for the sample Zr(C,N)_k_BL.....	57
Figura 24 – Residual stresses for the sample Zr(C,N)_k.....	58
Figura 25 – Residual stresses for the sample Zr(C,N)_k_BL and Zr(C,N)_ α	60

Figura 26	–	Integral line width for the $\alpha\text{-Al}_2\text{O}_3$ layer.....	61
Figura 27	–	Integral line width for the Zr(C,N) layer.....	62

LIST OF TABLES

Table 1- Properties of Al ₂ O ₃ layers investigated.....	18
Table 2- Samples selected for the work.....	37
Table 3 – Experimental parameters.....	39
Table 4 – Diffraction elastic constants for each sub-layer and substrate.....	42
Table 5 – (hkl) planes of maximum intensity for Zr(C,N).....	46
Table 6 – (hkl) planes of maximum intensity for Al ₂ O ₃	46
Table 7 – Results of residual stresses for the 111 and 222 planes in the Zr(C,N) layer.....	52
Table 8 – Elastic, thermal properties and theoretical residual stress for substrates and coating layers.....	63

SUMMARY

1.	PRELIMINARY RESULTS	15
2.	INTRODUCTION.....	16
3.	AIMS.....	19
4.	LITERATURE REVIEW.....	20
	4.1 Cemented carbides.....	20
	4.2 CVD process	21
	4.3 Coatings	22
	4.4 Residual stress	23
	4.5 X-ray stress analysis.....	25
	4.6 Energy dispersive X-ray diffraction	31
	4.7 Blasting process	32
	4.8 Milling operation.....	34
	4.9 Wear: Comb cracks	35
5	EXPERIMENTAL PROCEDURE.....	36
	5.1 Samples.....	36
	5.2 Residual stress	38
	5.2.1 EDDI station at BESSY.....	38
	5.2.2 Parameters for residual stress evaluation.....	40
	5.2.3 Crystallographic texture	42
6	RESULTS AND DISCUSSION.....	43
	6.1 Microstructural characterization.....	43
	6.2 ED Diffraction	45
	6.3 Crystallographic texture of CVD layers.....	46
	6.4 Residual stresses	48
	6.4.1 Effect of blasting in Zr(C,N)/ α -Al ₂ O ₃ layers at RT/800/RT thermal cycle.....	53
	6.4.2 Effect of Ti(C,N,O) bonding layer in Zr(C,N)/ κ -Al ₂ O ₃ layers at RT/800/RT thermal cycle	56
	6.4.3 Residual stress behaviour for Zr(C,N)/ κ -Al ₂ O ₃ and Zr(C,N)/ α -Al ₂ O ₃ layers with bonding layers at RT/800/RT thermal cycles	59
	6.4.4 Effect of the heating in the microstructure of each sub-layer.....	60
	6.4.5 Theoretical residual stresses of Zr(C,N), κ -Al ₂ O ₃ and α -Al ₂ O ₃	62

7 CONCLUSIONS..... 64
REFERENCES 66

1. PRELIMINARY RESULTS

The residual stress evolution in Ti(C,N)/ α -Al₂O₃ and Zr(C,N)/ α -Al₂O₃ CVD layers during thermal cycling has been investigated in previous work of the present author (MORENO,2017); (GARCÍA et al. 2017). This study has showed that:

- A cycling behavior of residual stress evolution can be observed for both systems studied: Ti(C,N)-based and Zr(C,N)-based.
- In the thermal cycling conditions (RT-800°C-RT), the Zr(C,N)-based system presented higher compressive stresses at 800°C and lower tensile stresses at RT compared to Ti(C,N) layer.
- The residual stress curve profile in the not-blasted condition is the same for the carbonitride and oxide layers for both systems. However the residuals stress values for Ti(C,N) layer are more tensile compared to the Zr(C,N) layer. The residual stress values were the same for the Al₂O₃ layer for both systems.
- For the complete thermal cycle in the blasted condition, the Zr(C,N) system presented more compressive stress than the Ti(C,N) system. As for the non-blasted condition the Zr(C,N) layer presented more compressive and less tensile behavior compared to the Ti(C,N) layer. The residual stress curve profile after the first temperature cycle was similar for both carbonitride and oxide layers.
- On blasted condition, the Al₂O₃ layer presented a high (and approximately constant) compressive stress in the first cycle in the two systems. And, after the first cycle, presented a similar behavior with the Ti(C,N) and Zr(C,N) layers.
- For the sample on the non-blasted condition the heating process does not affect the microstructure, independently if it is a Ti(C,N)-system or Zr(C,N)-system.
- In samples with blasted condition the annealing of intrinsic lattice defects was observed in Zr(C,N), Ti(C,N) and Al₂O₃ layers, indicating that the residual stress behavior may be influenced by the plasticity of the coating

layer systems.

Based on these conclusions about the systems evaluated it was decided investigate more about the thermal cycling behavior of Zr(C,N) layer, a promising material to replace Ti(C,N) in the cutting tools.

2. INTRODUCTION

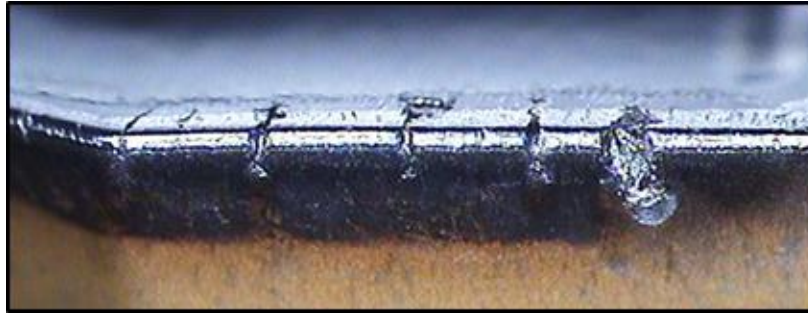
Cemented carbide (also known as hard metals) is a composite material manufactured by powder metallurgy, which consists of one or several hard components such as Tungsten Carbide embedded in a metallic binder, typically Co (GARCÍA et al. 2018).

During the 80's, the use of hard refractory metal carbide and aluminium oxide coatings led to a high improvement in cutting tool performance. Nowadays, hard metals are usually coated with thin films layers to improve their wear resistance (MITTERER, 2014). These thin films can be made of nitrides, carbonitrides and oxides varying in composition, thickness, texture, etc, depending on application (GARCÍA; PITONAK, 2013).

Titanium carbonitride (Ti(C,N)) is one of the most used materials for coatings due to its high hardness and chemical resistance (GARCÍA et al. 2010). Zirconium carbonitride (Zr(C,N)) is an alternative coating material to Ti(C,N), which presents excellent characteristics such as high hardness, elevated melting temperature and comparatively high electrical and thermal conductivities (IVASHENKO et al. 2009, EL AZHARI et al, 2018).

Coated cemented carbides are used for metal cutting. Milling is an intermittent machining operation which subjects the insert to interrupted thermo-mechanical loads. The cycling load leads to the formation of cracks (known as comb cracks). These cracks are initiated by the alternating expansion and contraction of the tool as it is heated and cooled during the interrupted cutting, shortening the tool life of cutting inserts (SADIK, 2014, GARCÍA et al, 2017). Fig. 1 shows a light optical stereographic image of comb cracks in the edgeline of milling inserts.

Figure 1: Comb cracks in milling inserts.



Source: García et al (2017)

The formation of comb cracks is affected not only by the thermomechanical cycling machining condition but also by the initial condition of the thin films after Chemical Vapor Deposition (CVD). Due to the high-temperature typically used in CVD processes (880-1050°C), the thin films are subjected to two important factors during the cooling step of the process that modifies the residual stress condition: a) the formation of thin cooling cracks forming a micro-network throughout the layer, and b) the evolution of tensile residual stresses (in the range of 0.3 to 0.8 GPa) due to the Coefficient of thermal expansion (CTE) mismatch between the thin films and the cemented carbide substrate (RUPPI; HALVARSSON, 1999).

In general, tensile stresses can lead to crack formation and propagation; thus, in order to prevent the crack formation, compressive stresses are usually beneficial to the tool components (GARCÍA et al, 2017). Reduced tensile stresses can be achieved using materials such as Zr(C,N), that present a reduced CTE compared to Ti(C,N), but also attractive properties such as, hardness, corrosion resistance and tribological performance comparable to Ti(C,N), which is the standard coating used in milling inserts (SILVA et al. 2010). In addition to the carbonitride layers, the multi-layer coating systems also contain a Al₂O₃ layer, which is applied as a thermal barrier for the tool. The alumina may be present in its stable form (α -Al₂O₃) or in its metastable form (κ -Al₂O₃), which can be obtained by varying the parameters in the CVD process. Alumina layer can be top-blasted to introduce compressive stresses of high magnitude (1.5 GPa) in the layers. It has been observed that because they have different crystalline structures (α -Al₂O₃ presents a hexagonal/trigonal structure whereas κ -Al₂O₃ presents an orthorhombic structure), they respond differently to top-blasting process, which also influences the resistance to deformation of the layer. κ -Al₂O₃ is more resistant to deformation compared to α -Al₂O₃.

Consequently its residual stress condition after top-blasting varies considerably, since compressive stresses cannot be achieved in κ - Al_2O_3 layers without damaging the integrity of the layers. The metastable κ - Al_2O_3 layer has an orthorhombic crystal structure formed from a pseudo-closed-packed stacking ABAC of oxygen atoms with Al in octahedral and tetrahedral environments in a 3:1 ratio. Due to the complex crystalline structure, lattice distortions can occur in different crystallographic directions leading to twinning as the predominant deformation mechanism in κ - Al_2O_3 phase in comparison with α - Al_2O_3 , in which dislocation is the type of recurrent defects observed (BARBATTI, et al. 2009).

Table 1 shows aluminium oxide properties for the different phases studied in this work.

Table 1: Properties of Al_2O_3 layers investigated

	α - Al_2O_3	κ - Al_2O_3
Stability	Stable	Metastable
Crystal system	Trigonal	Orthorhombic
Space group	R-3c	Pna2 ₁
Lattice parameters (Å)	Hexagonal (h) a = 4.7587, c = 12.9929, n = 6 Rhombohedral (R) A = 5.12, α = 55.17°, n = 2	a = 4.8351 b = 8.3109 c = 8.9363
Al atoms in unit cell	12 (h) / 4 (R)	16
O atoms in unit cell	18 (h)/ 6 (R)	24
CTE ($10^{-6}/\text{K}$) at RT	$\alpha(a) = 5$, $\alpha(b) = 6$	$\alpha(a) = 3.8$, $\alpha(b) = 5.1$, $\alpha(c) = 5.2$
E(GPa)	444 +- 20	344.3 +- 15.2
ν	0.21	0.24

Source: Halvarsson et al (1995); Rупpi (2005); Rупpi et al (2008); Accuratus (2013)

This also influences their technical application: α - Al_2O_3 -based systems are used in machining of steels, where wear-resistance and high compressive stresses are needed whereas κ - Al_2O_3 -based systems are used in for instance milling of cast iron where tougher layers are needed due to the abrasive character of the typical inclusions in these types of alloys (RUPPI, 2005).

Recently the author of this work investigated the effect of replacing

Ti(C,N) by Zr(C,N) on the high temperature residual stress behaviour of CVD coated milling inserts using “in-situ” synchrotron energy dispersive X-ray diffraction. The systems investigated were based on carbonitride layers combined with α -Al₂O₃. The conclusion was that systems containing thin carbonitride layers with reduced CTE (i.e. Zr(C,N)) developed higher compressive stresses during thermal cycling; which were of advantage to reduce the formation of thermo-mechanical cracks (GARCÍA et al. 2017).

In a further review of the literature on this subject it was observed that the understanding of the residual stress behaviour of coating systems based on κ -Al₂O₃ (both in terms of residual stresses and mechanical properties) is missing. κ -Al₂O₃ is an interesting coating that can be used as thermal barrier and should present higher ductility than α -Al₂O₃ due to its crystal structure. Nevertheless, no investigations on the in-situ residual stress development of κ -Al₂O₃ thin films were found, which justifies the relevance for this investigation.

The understanding of how residual and thermal stresses develop over temperature can help to avoid or minimize the appearance of comb cracks and increase the tool life of CVD coated milling inserts.

3. AIMS

The objectives of this work are to analyse residual stresses in multi-layer coatings produced by CVD on milling inserts, using ED synchrotron X-ray diffraction, in order to verify:

- the impact of surface post treatment after CVD coating deposition (micro-blasting) on the residual stress evolution of Zr(C,N)/ α -Al₂O₃ during the thermal cycle;
- comparison of in-situ the residual stress evolution in Zr(C,N)/ α -Al₂O₃ and Zr(C,N)/ κ -Al₂O₃ coatings in the thermal cycle;
- the effect of TiCNO bonding layer in the residual stress behaviour of Zr(C,N)/ κ -Al₂O₃ systems.

4. LITERATURE REVIEW

4.1 Cemented carbides

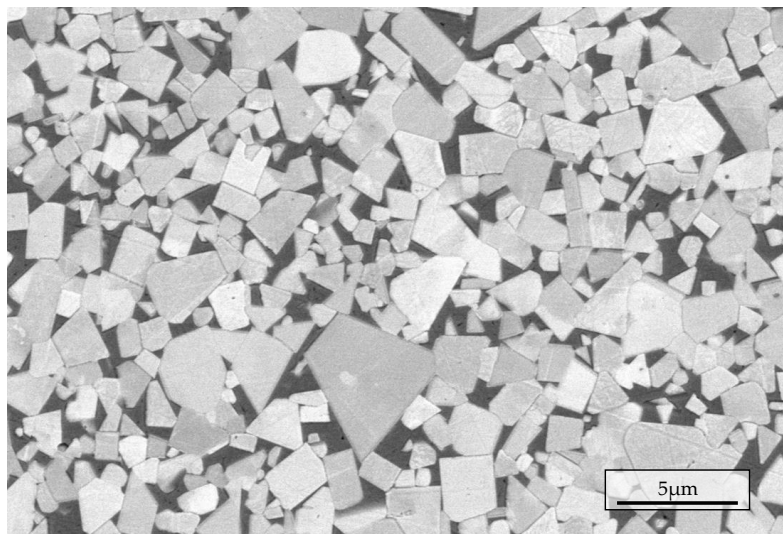
Cemented carbides or hard metals are the most common material used in the cutting tool industry due to their excellent combination of hardness and toughness compared to other cutting materials like carbon steels (GARCÍA et al, 2018). It is a powder metallurgy manufactured material which consists of one or several hard components such as Tungsten Carbide (WC) as the main component and a metallic binder, typically Co. Cemented carbides are produced by milling and mixing powders of these elements, compacting the mixed powder in different geometries followed by sintering at high temperature between 1300-1600°C (GARCÍA; STRELSKY, 2010). This manufacturing process ensures an excellent surface finish, produces inserts in the desired shape with tailored chemical composition and mechanical properties (TORRES; SCHAEFFER, 2008).

In this material, the hard phase offers high hardness and mechanical strength, whereas the binder phase has high toughness and plasticity. The final properties will depend of the amount added of each element. By selecting the appropriate combination of phases and processing parameters, different microstructures with a variety of mechanical properties can be achieved (GARCÍA et al, 2019).

For instance, the higher the Co-content, the lower the hardness and the higher the fracture strength is. The balance between hardness, toughness and wear resistance is the main objective to adjust mechanical properties (TORRES et al, 2009). Commercially, it has been used from 70 to 94% wt of the carbide phase and from 6 to 30% wt of Co (PRAKASH, 2014). The grain size of the cemented carbides can be varied in order to increase the wear resistance, usually between 0.1 and 5 μm (GARCÍA et al, 2019).

Fig. 2 illustrates a micrograph of a typical cemented carbide microstructure. The phases WC particles (white phase), and cubic carbides (rounded, grey) are embedded in the Co metal binder (black phase).

Figure 2: SEM image of a cemented carbide



Fonte: García et al (2019)

4.2 CVD process

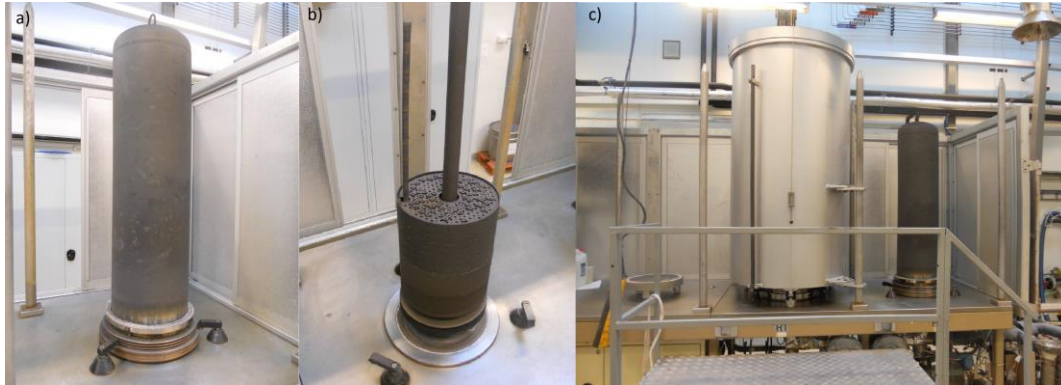
Cemented carbides are usually coated with ceramic multi-layers to improve their performance and wear resistance in cutting tools (MITTERER, 2014). There are several methods for coating deposition on tools, and the most commonly used process is CVD. This process can be defined as the deposition of a material on a heated surface from a chemical reaction in the vapor phase, and the deposited species can be atoms, molecules or a combination of these, forming a thin and solid film (PIERSON, 1999).

The equipment of CVD process consists of a vacuum-tight chamber. The inserts are loaded on to trays in a configuration such that the cutting tools are nearly touch one another. Some these trays are stacked on top of one another to form a “load”. The load is heated by radiation in the chamber, in order to maintain precise temperature control. Moreover, the CVD reactors for coating cutting tools contain several subsystems, including vacuum, gas handling, scrubbing and process control (REBENNE; BHAT, 1994).

The chemical reactions in the CVD process are activated thermally, and occurs at temperature between 900-1100°C and a strong adhesion is achieved due a good chemical and physical compatibility between the thin films and hard metal (LHERMITTE-SEBIRE I. et al, 1986).

Fig. 3 illustrates the CVD line, where a) shows the radial gas distribution in CVD and the trays with the inserts, b) the chamber closed and c) the chamber with the reactor, completing the CVD-coating line.

Fig. 3: CVD line



Source: Image courtesy Sandvik Coromant, Sweden

4.3 Coatings

In cutting tools applications multi-layers coatings made of nitrides and carbonitrides coatings are used to improve the wear resistance of tools due to their intrinsic properties (hardness and oxidation resistance). (GARCÍA; PITONAK, 2013).

Zirconium carbonitride ($Zr(C,N)$) is a material that has attracted the interest of researchers in recent years (IVASHENKO et al. 2009). $Zr(C,N)$ is a promising material for applications in extreme environments presenting excellent results when tested at different temperatures and pressures, correlating it good elastic properties, thermal expansion and Young's moduli compared to the most conventional $Ti(C,N)$ hard coating used in cutting tools (KIM; SUH, 2017).

Moreover, investigations on micro-mechanical properties of polycrystalline $Ti(C,N)$ and $Zr(C,N)$ coatings explained the high performance of $Zr(C,N)$ in cycling thermo-mechanical loads by the combination of high hardness, better cohesive strength and its intrinsic plasticity compared to $Ti(C,N)$ (EL AZHARI et al, 2018).

Alumina (Al_2O_3) is one of the materials most frequently deposited by CVD, and can be found in the forms $\alpha-Al_2O_3$, $\kappa-Al_2O_3$ and $\gamma-Al_2O_3$ being γ and κ , metastable phases (LARSSON; RUPPI, 2001).

Al_2O_3 is used as a heat barrier to avoid excessive heating of the cutting

tip and the early set up of plastic deformation, due its high chemical and thermal stability. Moreover, this coating act as a barrier protecting the hard metal from dissolution thus reduces the crater wear on the tool. However, due to the sliding of workpiece material against the rake and flank faces the relatively soft Al_2O_3 is exposed to wear which limits the tool life. Consequently, alternatives have been made to improve the properties of CVD Al_2O_3 coatings, e.g. through the deposition of different types of Al_2O_3 , $\kappa\text{-Al}_2\text{O}_3$ rather than $\alpha\text{-Al}_2\text{O}_3$ (FALLQVIST; OLSSON; RUPPI, 2007) or through refinement of crystallite size or preferred texture (GARCÍA, 2016).

Some advantages are observed in the use of $\kappa\text{-Al}_2\text{O}_3$. This coating can have smaller grain size and lower porosity than $\alpha\text{-Al}_2\text{O}_3$. Hence, in the cutting tool application the $\kappa\text{-Al}_2\text{O}_3$ may exhibit high hardness due its defect free structure and lower thermal conductivity, in addition to epitaxial growth, being beneficial to the inserts as a thermal barrier (RUPPI; HALVARSSON, 1999).

4.4 Residual stress

Residual stresses can appear in materials during any step of processing, for example when it is subjected to heat treatment or machining or even by chemical treatment (NOYAN; COHEN, 1986); (PERRY et al, 1996).

These stresses act within the materials without the external loads at room temperature. In metallic materials they usually occur due to inhomogeneous plastic deformation, however, this can also occur due to temperature variations when two or more materials that have different CTE are in contact, as it is the case of the inserts coated with multi-layers (LAGATTA, 2011). In addition, the residual stresses can be originated due to a gradient of chemical composition in the coating and/or substrate (CAMPOS; MACHADO; HIRSCH, 2006).

CVD coatings can exhibit residual stresses, depending on the temperature deposition and materials used to coating and substrate (HIRSCH; MAYR, 1988). In this case, the CVD process presents an extrinsic stress due to the different thermal contraction between the thin film and cemented carbide, which is inherent in the deposition and can be tensile or compressive. (PERRY et al, 1996). Different types

of stresses can be observed in coatings and can be classified as below:

1. Macro-stresses appearing from the coating growth and from the thermal expansion incompatibility;
2. Micro-stresses induced by the plastic and elastic anisotropy between grains and sub-grains;
3. Micro-stresses arising from dislocation and point defects causing fluctuations of the lattice parameter. (SKRZYPEK et al, 2001)

The effect of each type can be beneficial or not, depending on their magnitude, signal, and distribution. In many cases the residual stresses can be harmful, because they overlap the service stresses. However, when it is desired to increase the fatigue stress limit, for example, compressive stresses are introduced into the surface by blasting (RIBEIRO, 2006).

Compressive residual stresses generally have a beneficial effect on the fatigue life, crack propagation or stress corrosion. Tensile stresses on the other hand, decrease the material performance under the same conditions (SUTERIO, 2005). If a high tensile stress occurs, cracks may develop or delamination on coating is observed (LAGATTA, 2011).

Residual stresses in thin films can be classified into two types:

- Intrinsic stresses (σ_i): arise during the growth of the film, sometimes by defects incorporated in the structure of the films.
- Extrinsic stresses (σ_e): appear after the growth of the film, mainly by the difference between the thermal expansion coefficients of the film and substrate. This represents the main contribution in case of CVD (MADY et al. 2008).

A stress that also can occur in the component is called thermal stress. This stress develops in CVD process due to thermal expansion or contraction of a homogeneous material in a temperature gradient field (ERICSOON, 2014). The extrinsic stress in CVD process can be considered a thermal macro-stress (KEWEI et al, 1993). Polycrystalline ceramics also presents thermal stress due to the crystallographic misorientation across the grain boundaries (VEDULA et al, 2001).

There are many methods for analysing residual stresses that can be classified into semi-destructive, destructive, and non-destructive. The first two act in order to alter the equilibrium state of the stresses, causing them to be relieved in the measured region. Non-destructive methods are based on the variations of physical or crystallographic parameters of the material under analysis (SUTERIO, 2005). For thin

film measurements, non-destructive techniques are usually used. Currently two categories have been highlighted: one is based on the direct measurement of elastic lattice deformations by X-ray diffraction, and another one uses the deflection or curvature of the substrate induced by the stress within the layer (TAVARES, 1997).

4.5 X-ray stress analysis

The investigation of residual stresses in the cutting tool industry is very important to analyse the thin films, due the influence of these stresses in the properties of the inserts. X-ray diffraction has proven to be the most efficient method to evaluate the properties and structure of polycrystalline materials (NOYAN et al, 1995); (PERRY; JAGNER, 1989).

Owing to the larges sample series and their process control in the industry, there is an increase of the use of the X-ray stress analysis (XSA) in comparison with the non-diffraction methods for polycrystalline materials, despite of the extensive measurement time. Moreover, this method presents advantages to obtain information of the complex residual stress fields in the near surface region of the thin films (GENZEL, 2001).

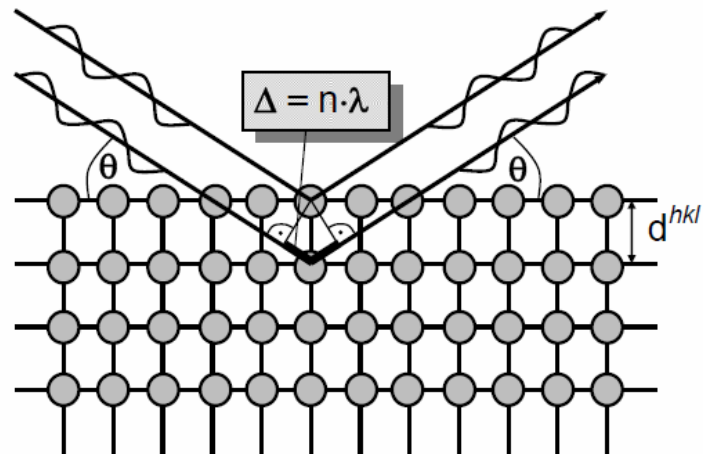
Polycrystalline materials consist of individual crystallites with a certain irregular distribution of their orientations. Since the crystalline state is characterized by a strict spatial ordering of the atoms, the spacings between the lattice planes can be determined experimentally by means of the Bragg equation in its angle dispersive (AD) form:

$$\lambda = 2d^{hkl}\sin\theta^{hkl} \quad \text{Eq.(1)}$$

In Eq. (1) λ denotes the wavelength of the radiation, d^{hkl} the lattice spacing to be determined and θ^{hkl} the Bragg angle. The Miller indices hkl characterize the orientation of the investigated lattice planes with respect to the crystal reference system. From the relation (1) it follows immediately that the Bragg angle, under which reflection is observed, depends on the crystal structures of the material. Therefore, X-ray diffraction can be used to identify individual phases of a multiphase material. The principle of Bragg reflection is shown in Figure 4. Constructive interference is observed

in form of a diffraction line, if the path difference Δ of two neighboring rays is equal to a multiple of the wavelength period λ .

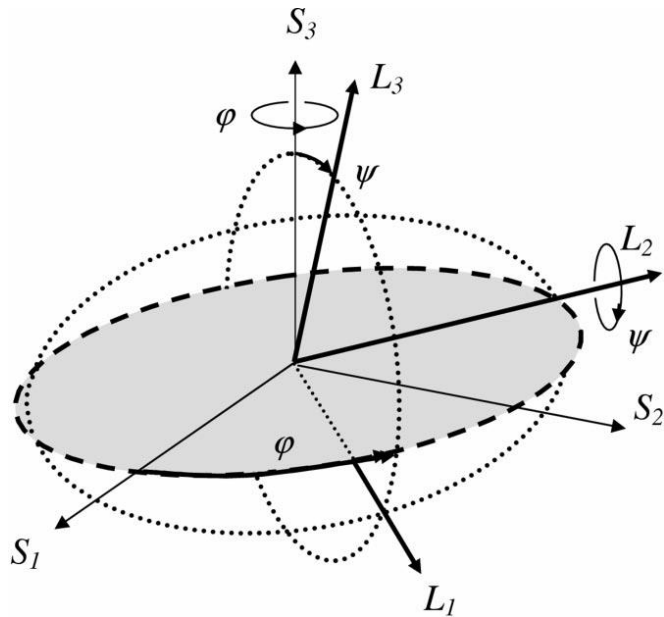
Figure 4: The principle of Bragg reflection.



Source: Genzel et al. (2015-2017)

X-ray stress analysis uses the fact that elastic stresses cause a lattice strain, i. e. a variation of the lattice spacings within the crystallites, which leads to a measurable shift of θ^{hkl} according to (1). The geometrical situation is shown below in figure 5.

Figure 5: Definition of the sample reference system (S) and the laboratory system (L) in X-Ray analysis. (φ, ψ) denote the azimuth and inclination angle, respectively, of the measuring direction L_3 with respect to S



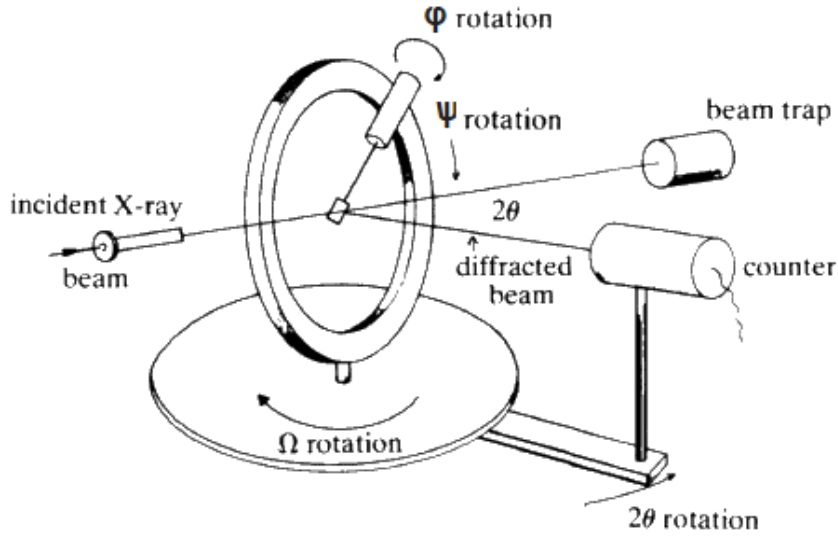
Source: (Welzel et al, 2005)

If (S) denotes the sample reference system, the correlation between the lattice strain $\varepsilon_{\psi\varphi}^{hkl}$ of the diffracting crystallites within the gauge volume measured in any direction (φ, ψ) with respect to (S) and the components of the residual stress tensor $\langle \sigma_{ij}^S \rangle$ also related to the S-system and averaged over all crystallites is given by the so-called fundamental equation of XSA (Eq. 2):

$$\varepsilon_{\psi\varphi}^{hkl} = \frac{d_{\psi\varphi}^{hkl} - d_0^{hkl}}{d_0^{hkl}} = \frac{1}{2} S_2^{hkl} \sin^2 \psi [\langle \sigma_{11}^S \rangle \cos^2 \varphi + \langle \sigma_{22}^S \rangle \sin^2 \varphi + \langle \sigma_{12}^S \rangle \sin 2\varphi] + \frac{1}{2} S_2^{hkl} \sin^2 \psi [\langle \sigma_{13}^S \rangle \cos \varphi + \langle \sigma_{23}^S \rangle \sin \varphi + \langle \sigma_{33}^S \rangle \cos^2 \psi] + [S_1^{hkl} (\langle \sigma_{11}^S \rangle + \langle \sigma_{22}^S \rangle + \langle \sigma_{33}^S \rangle)] \quad \text{Eq. (2)}$$

Where d_0^{hkl} is the lattice spacing of the strain-free material, and φ and ψ denote two rotation angles of an X-ray diffractometer. Fig. 6 shows a 4-circle X-ray diffractometer, where it is possible to visualize its rotation angles, including φ and ψ .

Figure 6: Schematic view of X-ray diffractometer



Source: Science Education Resource Center (2007)

In Eq. (2) S_1^{hkl} and $\frac{1}{2}S_2^{hkl}$ are the diffraction elastic constants (DEC), which depend on the investigated reflection hkl , and, therefore, on the single crystal elastic anisotropy of each phase, $S_1^{hkl} = \frac{\nu^{hkl}}{E^{hkl}}$ and $1/2S_2^{hkl} = \frac{1+\nu^{hkl}}{E^{hkl}}$, where ν^{hkl} is the Poisson's ratio and E^{hkl} is the Young's modulus specific for each hkl (GNÄUPEL-HEROLD et al. 2012); (PERRY, et al, 1992).

The DEC's are typically calculated using the single-crystal elastic constants and follow grain-grain interaction models such Voigt, Reuss, Hill and Eshelby-Kröner.

The Voigt model assumes that the all grains in the polycrystalline material possess strain tensors that are equal to the macroscopic strain tensor. The result is an average over all crystal orientations, yielding an isotropic tensor. For the cubic structure and absence of crystallographic texture is obtained (MURRAY, 2013):

$$S_{1Voigt}^{hkl} = -\frac{S_0(S_{1111}^C + 2S_{1122}^C) + 10S_{1122}^C S_{1212}^C}{3S_{1111}^C - 3S_{1122}^C + 4S_{1212}^C} \quad \text{Eq. (3)}$$

$$\frac{1}{2}S_{2Voigt}^{hkl} = \frac{10S_{1212}^C(S_{1111}^C - S_{1122}^C)}{3S_{1111}^C - 3S_{1122}^C + 4S_{1212}^C} \quad \text{Eq. (4)}$$

Where S_0 refers to the compliance tensor and S_{ijkl}^C represent the

components of the fourth-rank compliance tensor.

The Reuss model assumes that all crystallites possess identical stress tensors, but that the strain tensors do not need to be equivalent. For the cubic structure and absence of texture, the DEC's are obtained with the following equations (MURRAY, 2013):

$$S_{1\text{Reuss}}^{hkl} = S_{1122}^C + S_0 \Gamma \quad \text{Eq. (5)}$$

$$\frac{1}{2} S_{2\text{Reuss}}^{hkl} = S_{1111}^C - S_{1122}^C - 3S_0 \Gamma \quad \text{Eq. (6)}$$

The eq. 5 and 6 depend linearly on the orientation parameter, Γ

$$\Gamma = \frac{h^2 k^2 + h^2 l^2 + k^2 l^2}{h^2 + k^2 + l^2} \quad \text{Eq. (7)}$$

An average of the Reuss and Voigt model was proposed by Neerfeld and Hill, and is known as Neerfeld-Hill model (BACZMANSKI et al. 1995):

$$S_{1\text{Hill}}^{hkl} = \frac{(S_{1\text{Voigt}}^{hkl} + S_{1\text{Reuss}}^{hkl})}{2} \quad \text{Eq. (8)}$$

$$\frac{1}{2} S_{2\text{Hill}}^{hkl} = \frac{\frac{1}{2} S_{2\text{Voigt}}^{hkl} + \frac{1}{2} S_{2\text{Reuss}}^{hkl}}{2} \quad \text{Eq. (9)}$$

The DEC's are orientation-selective averages over a subset of all grains, and therefore these dependencies remain valid to a degree. In addition, from Eshelby's theory it is known that the strain/stress response of a single grain depends on the elastic properties of its surrounding as well as of its shape (ESHELBY, 1957). The preferred orientation of grains can also have a profound effect on the magnitude and orientation. The Eshelby-Kröner model is the only model that can account for all of these effects in the DEC. (GNÄUPEL-HEROLD et al. 2012). Hence it was the model chosen in this work.

Eqs. 10 and 11 show the relations for cubic phases with nearly random distribution of grain orientations:

$$S_{1EK}^{hkl} = S_1^B + t_1 + t_0\Gamma \quad \text{Eq. (10)}$$

$$\frac{1}{2}S_{2EK}^{hkl} = 2S_2^B + 2t_2 + t_0(1 - 3\Gamma) \quad \text{Eq. (11)}$$

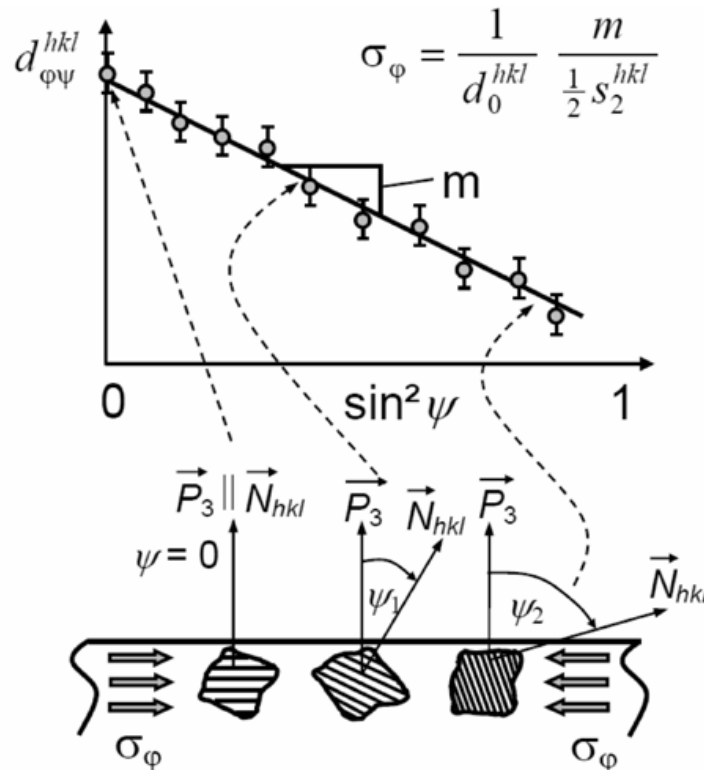
In this case $t_0 = t_{1111} - t_{1122} - 2t_{1212}$, $t_1 = t_{1122}$ and $t_2 = t_{1212}$, t_{ijkl} are the component of the elastic susceptibility tensor that represents the elastic interaction of a crystal in an elastic matrix.

Because the information depth of the X-rays within most of the materials is only a few microns, Eq. (2) simplifies in many cases considerably. Thus the stress components σ_{i3} ($i = 1,2,3$) perpendicular to the surface can be neglected in the evaluation, if the boundary conditions $\sigma_{i3}(z = 0) \equiv 0$ valid at the free surface are assumed to be approximately fulfilled within the total irradiated depth below the surface. In this case Eq. (2) turns into Eq (12):

$$\varepsilon_{\psi\varphi}^{hkl} = \frac{1}{2}S_2^{hkl}\sigma_\varphi\sin^2\psi + 2S_1^{hkl}(\sigma_{11} + \sigma_{22}) \quad \text{Eq. (12)}$$

$\sigma_\varphi = \sigma_{11}\cos^2\varphi + \sigma_{22}\sin^2\varphi + \sigma_{12}\sin 2\varphi$ is the in-plane residual stress component in the azimuth direction φ . If the lattice spacings d^{hkl} are determined according to Eq. (1) for different inclination angles ψ between the surface normal \mathbf{S}_3 and the measuring direction $L_3 \parallel \mathbf{g}^{hkl}$ (\mathbf{g}^{hkl} – normal vector of the diffracting lattice planes), then it becomes clear from Figure 5 that the distance between the lattice planes depends on ψ , or in other words, on their orientation with respect to the direction of the stress acting in the material.

For example, if the in-plane stress state is compressive within the information depth of the X-rays, from Figure 7, the lattice spacings parallel to the surface ($\psi = 0$) are increased by the effect of transverse expansion, whereas those having a large inclination with respect to the surface ($\psi = \psi_2$) are compressed due to the direct influence of σ_φ . Thus, plotting the lattice spacings $d_{\varphi\psi}^{hkl}$ or the strains $\varepsilon_{\varphi\psi}^{hkl}$, respectively, against $\sin^2\psi$ it follows immediately from equation (11), that the slope of a regression line fitted to the $d_{\varphi\psi}^{hkl}$ vs. $\sin^2\psi$ distribution is proportional to the amount of the residual stress component σ_φ .

Figure 7: The principle of the $\sin^2\psi$ method for the analysis of residual stress

Source: Genzel et al. (2015-2017)

One of the most important advantages of this so-called $\sin^2\psi$ method is given by its numerical stability and insensitivity to experimental uncertainties. So the exact knowledge of the strain-free lattice spacing d_0^{hkl} , which is often very difficult to obtain, is only of minor importance in this case, because the stress evaluation is based on a *relative* comparison of lattice parameters.

4.6 Energy dispersive X-ray diffraction

Energy dispersive X-ray diffraction (ED-XRD) differs from conventional X-ray diffraction by using polychromatic photons as the source and is usually operated at a fixed angle. With no need for a goniometer, ED-XRD is able to collect full diffraction patterns very quickly. ED-XRD is almost exclusively used with synchrotron radiation which allows for measurement within real engineering materials. ED-XRD generates a complete diffraction spectra with reflexions for sample and detector in fixed points. Jointly with the high flux of synchrotron radiation is observed a wide range of study possibilities in materials science (GENZEL et al, 2007). The advantages of EDXRD

are: it uses a fixed scattering angle, it works directly in reciprocal space, it provides fast collection time and parallel data collection.

In ED-XRD the radiation is polychromatic and the scattering angle 2θ , under which diffracted energy spectrum is observed, can be chosen freely and remain fixed during the measurement. The correlation between the lattice spacing d^{hkl} and the corresponding diffraction line E^{hkl} on the energy scale follows immediately by inserting the energy relation $E = h\nu = hc/\lambda$ into the Bragg equation

$$d^{hkl} = hc/(2 \sin \theta E^{hkl}) = \text{const.}/E^{hkl}, \quad \text{Eq.(13)}$$

(h - Planck's constant, c - velocity of light). The lattice strain $\varepsilon_{\varphi\psi}^{hkl}$ determined at some orientation (φ, ψ) with respect to the sample system becomes

$$\varepsilon_{\varphi\psi}^{hkl} = (d_{\varphi\psi}^{hkl} - d_0^{hkl})/d_0^{hkl} = (E_0^{hkl} - E_{\varphi\psi}^{hkl})/E_{\varphi\psi}^{hkl} = \Delta E_{\varphi\psi}^{hkl}/E_{\varphi\psi}^{hkl}, \quad \text{Eq.(14)}$$

where E_0^{hkl} denotes the energy that corresponds to the strain-free lattice spacing d_0^{hkl} . Besides the higher information depths achieved in ED diffraction experiments, the multitude of reflections recorded in one energy spectrum is an important additional parameter that can be used in the depth-resolved XSA. From equation (13) it follows immediately, that the diffraction line profiles E^{hkl} of smaller lattice spacings are recorded at higher energies if the diffraction angle θ is kept fixed. Consequently, if strain depth-profiling is performed in the same (geometrical) way as in the XSA, the individual $\varepsilon_{\varphi\psi}^{hkl}(\tau)$ profiles evaluated for different hkl come from different average depth ranges, which usually overlap each other. Plotting the residual stress values which were evaluated for any reflection hkl from the slopes of $d_{\varphi\psi}^{hkl}$ vs. $\sin^2 \psi$ curves versus some average information depth

$$\langle \tau^{hkl} \rangle = [\tau(\psi_{min}, E^{hkl}) + \tau(\psi_{max}, E^{hkl})]/2 \quad \text{Eq.(15)}$$

one obtains a first approximation $\sigma_{ij}(\langle \tau^{hkl} \rangle)$ for the depth distribution of the in-plane stresses. (GENZEL et al, 2015-2017).

4.7 Blasting process

Many techniques have been developed to improve the lifetime of cutting

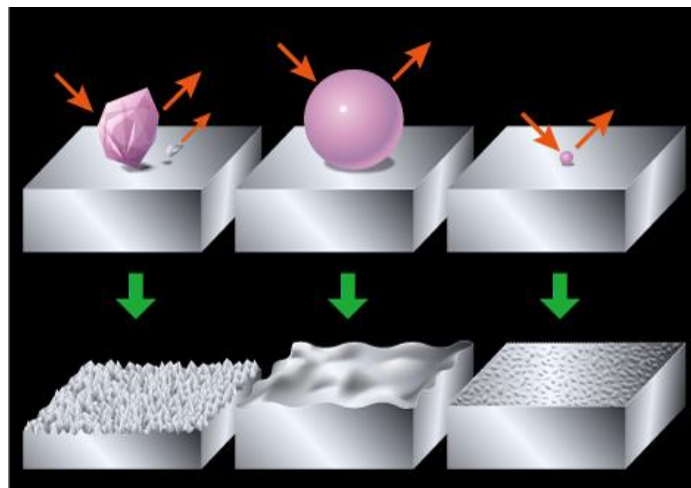
tools such as heat treatment, surface coating, and surface shape design, for example. Bombardment with millions of micro-particles ranging in size from 4 to 50 μm with a controlled process can lead to improvement of the cutting tool life (KENNEDY et al. 2005) This process is called blasting or more appropriately, micro-blasting or top-blasting.

Micro-blasting is a kind of finishing process that is based on the impact treatment of the surfaces. This technique uses high pressure and abrasives powders, for example Al_2O_3 and zirconium oxide (ZrO_2). It is applied to coatings to clean, smooth the surface and to reduce sharp cutting edges (BARBATTI et al. 2009). It is a method to change the micro topography as well as the surface integrity of tools. Surface effects of micro blasting depend among other parameters on the grain size of the blasting material (TÖNSHOFF et al., 1998). Fig. 8 presents the different particles and the effect on the surface of the material.

This post-treatment is normally used to modify the tensile stresses in the surface region on the thin films (BARTOSIK; PITONAK; KECKES, 2011). A beneficial effect is an introduction of compressive residual stresses (BARBATTI et al. 2009). These compressive residual stresses are the ideal of “residual stress engineering” within the coating systems (KLAUS; GENZEL; HOLZSCHUCH, 2008).

The process contributes to improve the coating adhesion, reduce the friction between workpiece and film and decrease the toughness improving the performance of coated cutting tools (BOUZAKIS et al. 2005) (GARCIA et al, 2014). (RIEDL, et al 2012).

Figure 8: Different blasting particle types and effects on surface of materials

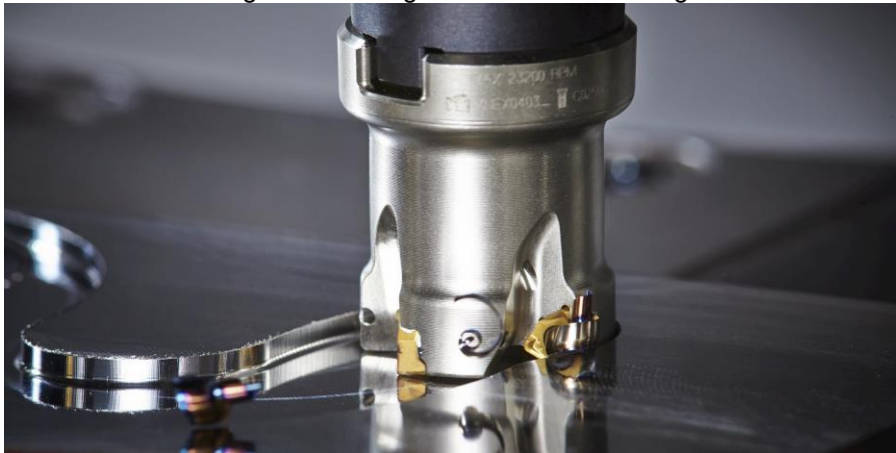


Source: WPC Treatment (2015)

4.8 Milling operation

Milling is an intermittent machining operation which is used to generate a flat or a three-dimensional free-formed surface (KARAGUZEL, et al 2006). The material is removed in a direction perpendicular to the axis of the cutter by a rotating multiple-tooth cutter and the workpiece is attached to a moving table and fed towards the cutter, thus forming and removing chip each time a tooth enter the material (TRENT; WRIGHT, 2000) (ADNAN, M. et al. 2015). Fig. 9 displays a milling tool.

Figure 9: Cutting tool used in the milling



Source: Seco Tools (2019)

The temperature and the stress intermittence at the machining conditions has a direct effect on the inserts. During the process, the cutting edge goes from being engaged with the workpiece, to disengaging from the workpiece cyclically. The temperature increases as the tool is active and decreases as the tool leaves the workpiece. This causes an expansion and contraction of the surface of the cutting edges. The temperature gradient causes tensile and compressive stress cycles that affect the tool, limiting the tool life (MELO et al. 2006). The milling process has a good efficiency, because it has a high capacity to remove material and to form short chips to machine pieces with excellent finishing. However, to achieve this performance, it is necessary to have extremely modern machines that support the inherent mechanical loads of the process, due to the moments when the tool is active and inactive (MELO, 2001).

The operation can be done with cutting fluid or not. When milling uses

coolant media during the machining the temperature gradient will be larger than when milling without coolant (SADIK 2014). So, avoiding cutting fluid can be beneficial to reduce the stresses caused by the temperature, but may lead to other type of wear mechanisms, such as plastic edgeline deformation.

4.9 Wear: Comb cracks

Cemented carbides tools frequently have your life shortened in interrupted cutting e.g. milling compared with continuous machining in the same work conditions. It was observed when they act in a thermal cycling (heating and cooling) cracks appears on the face tool of the insert (BATHIA; PANDEY; SHAN, 1978). This alternation causes temperature fluctuations, and this leads to an intense wear tool, generating cracks, so-called comb cracks or thermomechanical cracks. The crack development and propagation is the principal type of wear and failure of cutting tools in intermittent operations (BATHIA; PANDEY; SHAN, 1980).

These thermo-mechanical fluctuations associated with intermittent cutting cause variations of stress as a consequence of the difference CTE between the substrate and the coating layer. This may lead to the formation of the comb cracks perpendicular to the cutting edge and with regular distances, hence giving the edge a comb-like appearance (GARCÍA et al. 2017).

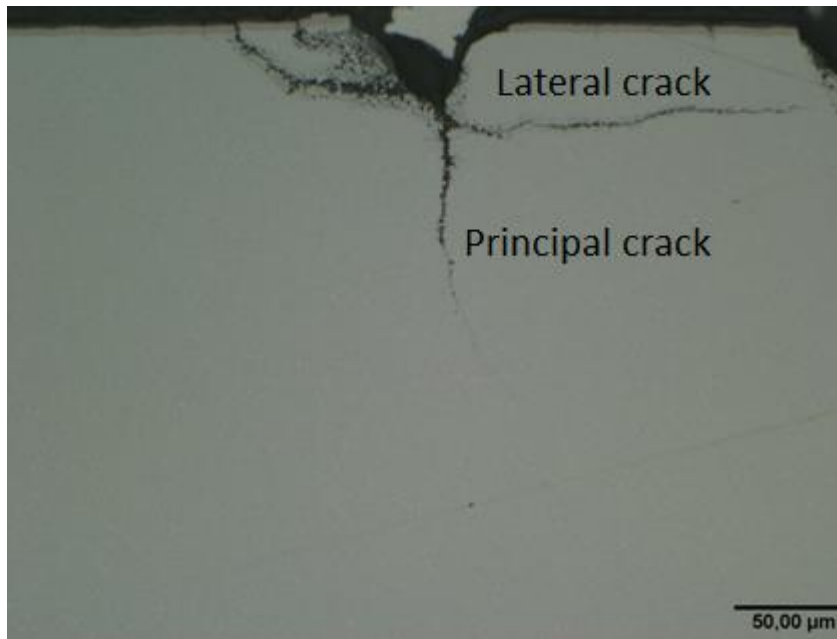
In addition, the variation of temperature depends on some parameters of the milling process, such as feed rate, cutting depth speed and the material that the workpiece and the insert was manufactured from (SADIK 2014). Due the high temperature in the CVD process (1000°C), tensile residual stresses are generated in the thin films; and this contributes to the formation of cracks and this affects negatively the tool performance and life as it decreases the mechanical stability of the coating (TKADLETZ, M. et al. 2015).

The comb cracks grow following certain stages. Initially, the cracks form in the coating, and in this stage the wear is mainly influenced by the temperature. As a consequence of this, the cracks are named thermal cracks. Afterwards, these cracks propagate into the substrate (GARCÍA et al. 2015b).

The morphology of comb cracks was investigated and depends if the milling operation was performed with or without cooling media. During milling with

cooling media, cracks develop from the initial (principal) crack, forming lateral cracks, parallel to the cutting edge with a semi-circular shape. However in the operation without cooling, these lateral cracks do not develop (GARCIA et al. 2015b). Fig. 10 illustrates the comb cracks with the principal and the lateral crack.

Figure 10: Comb crack - principal and lateral crack

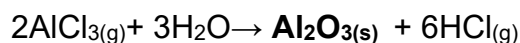
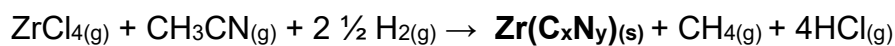
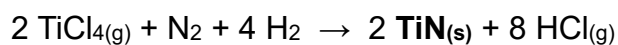


Source: GARCÍA et al. (2015b)

5 EXPERIMENTAL PROCEDURE

5.1 Samples

The samples studied in this work were coated using CVD in the laboratory of Sandvik Coromant R&D. The starting TiN layer, the intermediate Zr(C,N) layer, the Ti(C,N,O) bonding layer, and both the α -Al₂O₃ and κ -Al₂O₃ coatings were produced by state-of-the-art CVD processes by following chemical reactions:



where (s) means a solid phase and (g) gas phase.

The reaction takes place at a temperature range between 750 and 950 °C; for this reason the process is called “moderate” or “medium” CVD. The reactor pressure varies between 15 and 150 mbar. For deposition temperatures of around 900 °C, the composition is almost fixed to 50 at% C and 50 at% N, so that a $Zr(C_{0.5}N_{0.5})$ coating layer form.

The microstructure characterization was carried out using a field-emission gun (FEG) Scanning Electron Microscopy (SEM), Helios 40, to verify the integrity of the layers.

Table 2 presents the samples that were selected for the present work, and their characteristics. Stress analyses were conducted in-situ using synchrotron X-rays during thermal cycling where RT1 stands for room temperature before the heat treatment, 800°C is the high temperature achieved (typical working peak temperature of cutting tools) and RT2 is room temperature after the heat treatment, this cycle was repeated three times. The substrate composition was WC-6wt%Co with a grain size of 0,74 μm .

Tables 2: Samples selected for the work

Name	Composition	Thickness	Blasting
ZrCN_α	TiN + ZrCN+ TiCNO + α-Al ₂ O ₃	4/4 μm	No
ZrCN_α_b (b= blasted)	ZrN + ZrCN+ TiCNO + α-Al ₂ O ₃	4/4 μm	Yes
ZrCN_κ	TiN + ZrCN + κ-Al ₂ O ₃	3/3,1 μm	No
ZrCN_κ_BL (BL= bonding layer)	TiN + ZrCN + TiCNO + κ-Al ₂ O ₃	3,6/3,6 μm	No

Source: The author

Fig. 11 shows the kind of insert analysed in this work, and the location where in-situ stress analyses were conducted.

Figure 11: Insert for the stress analyses



Source: The author

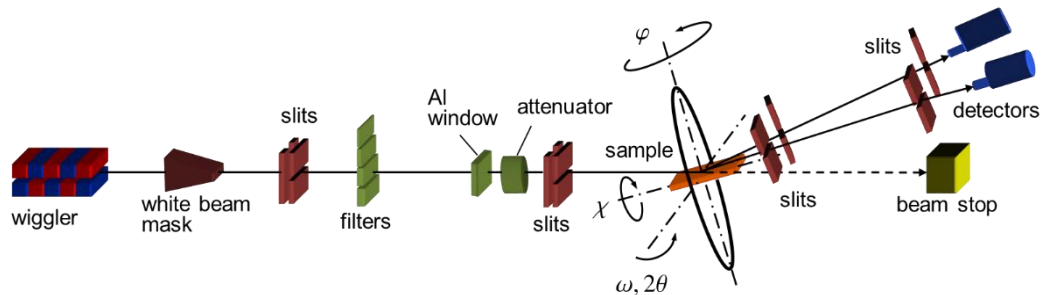
5.2 Residual stress

5.2.1 EDDI station at BESSY

Investigations using the energy dispersive mode of diffraction can be carried out at the Helmholtz-Zentrum Berlin (HZB) at the materials science beamline EDDI (*Energy Dispersive Diffraction*), which is operated at the Berlin synchrotron storage ring BESSY II.

The energy dispersive method can be used because it is possible to measure several crystallographic planes simultaneously. Fig. 12 shows the setup of the equipment at HZB. The high energy X-ray beam is provided by a 7T multipole wiggler, which emits photons within an energy range of 8-120 keV in a horizontal fan of some degree but highly collimated in the vertical plane. The optical elements of the beamline consist of an absorber mask to predefine the primary beam cross-section, a filter system to attenuate low energy photons giving rise to sample heating due to absorption and a cross-slit system to define the final beam shape. The primary beam meets the sample, which can be mounted on different sample positioning units that enable to realize any diffraction geometry applied in stress and texture analysis.

Figure 12: Schematic view of the components of the EDDI beamline



Source: Genzel et al. (2007)

The beamline is controlled by the software SPEC and for the preparation of measurements as well as for data evaluation MATHEMATICA and MATLAB programs are available. MATHEMATICA program was developed for processing ED diffraction data (GENZEL et al, 2007). The experimental parameters that were used at the EDDI beamline are summarized in the Tab. 3.

Table 3: Experimental parameters.

Primary beam	0.5 x 0.5 mm ²
Absorber	---
Secondary optics	double slit system 0.03 x 8 mm ² (equatorial x axial), $\Delta 2\theta < 0.01^\circ$
Diffraction angle	$2\theta = 9^\circ$
XSA-Mode	symmetrical ψ -Mode (reflection), $\psi = 0^\circ \dots 77^\circ$, $\Delta(\sin^2 \psi) = 0.1$
Detector	Low energy solid state Ge detector (Canberra Model GL0110)
Counting time	100 s
Calibration	gold powder (standard specimen on glass plate)

Source: Genzel et al. (2017)

For the high temperature investigations, a heating station DHS 1100 (Anton Paar) that was developed especially for X-ray diffraction experiments was used. The device is equipped with two thermocouples, one to control the default (set)

temperature of the heater and one to control the actual temperature on the sample surface where the diffraction measurement is performed.

5.2.2 Parameters for residual stress evaluation

The individual diffraction lines were evaluated by least-squares fitting of the data with the pseudo-Voigt function. About this function, the reader is referred to (SANCHEZ-BAJO; CUMBRERA, 1997). The diffracted intensities were corrected for various factors such as absorption, Lorentz and polarization factor (LPA correction), and in case of energy-dispersive measurements additionally for the wiggler spectrum and detector dead time induced diffraction line shifts. For detailed information regarding the correction of X-ray intensities, the reader is referred to (GENZEL et al, 2015-2017)

The diffraction elastic constants (DECs) required for the evaluation of the residual stresses and stress depth profiles were evaluated by the Eshelby-Kröner model, using the respective single crystal elastic constants.

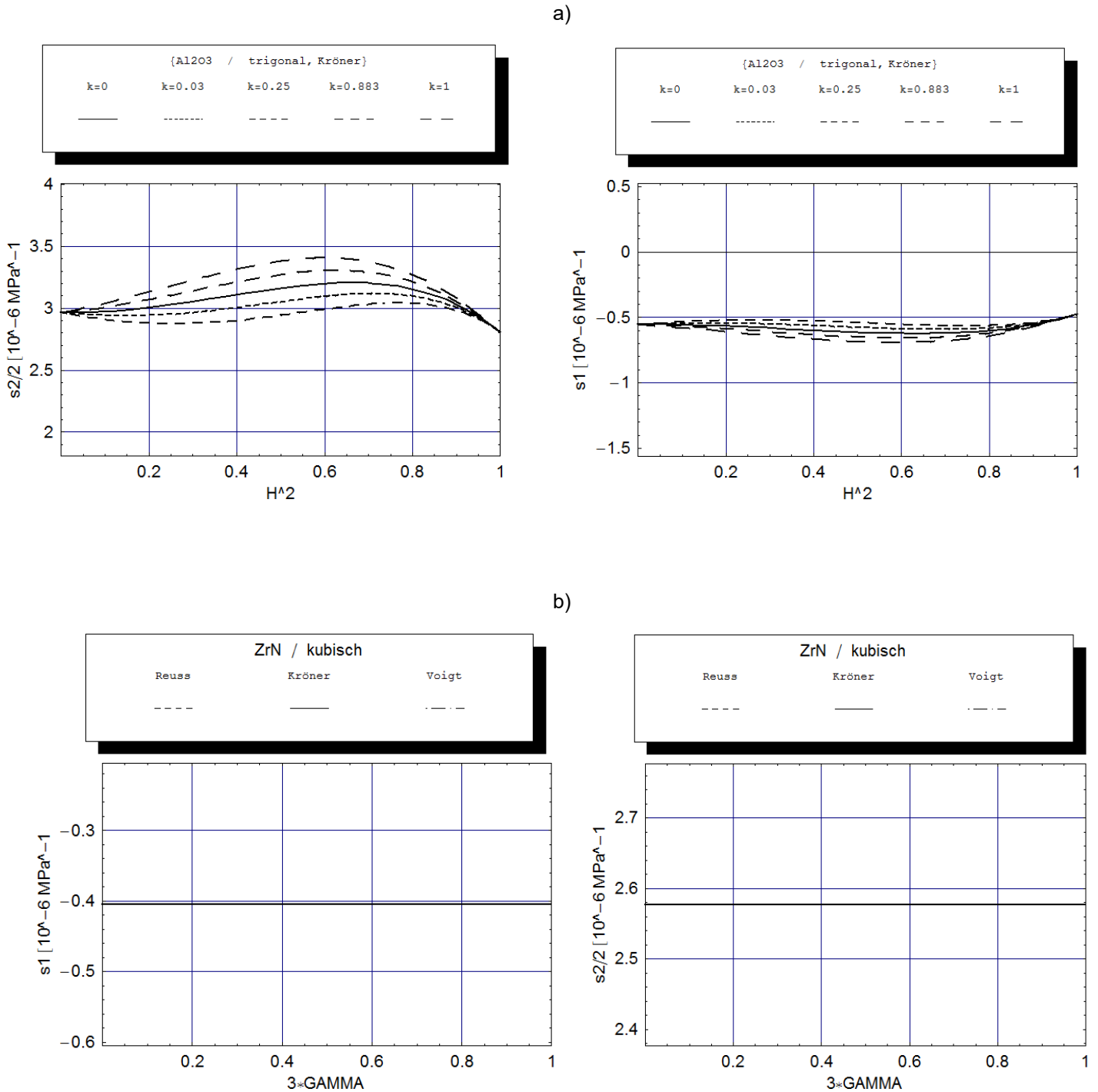
The results for $\frac{1}{2}S_2^{hkl}$ and S_1^{hkl} of the materials $\kappa\text{-Al}_2\text{O}_3$, and ZrN (component of Zr(C,N)) studied in this work can be seen in the Figure 13. For cubic crystal symmetry (like in the present case) the DEC are plotted versus the orientation factor:

$$3\Gamma = 3(h^2k^2 + k^2l^2 + l^2h^2)/(h^2 + k^2 + l^2)^2 \quad \text{Eq. (16)}$$

for crystals with hexagonal symmetry the orientation factor is given by

$$H^2 = 3l^2/[4(c/a)^2(h^2 + k^2) + 3l^2] \quad \text{Eq. (17)}$$

Figure 13: Diffraction elastic constants of a) Al_2O_3 , b) ZrN calculated by the models of Voigt, Reuss and Eshelby-Kröner



Source: Genzel et al. (2015-2017)

Figure 13 shows that the elastic anisotropy is negligible for all layer types. For the stress evaluation in the $\text{Zr}(\text{C},\text{N})$ layer it was noted that the DEC for ZrC is very

similar to those shown for ZrN in the Figure 13. Thus, an average of these values can be used, and the table 4 shows the values used for all lattice planes investigated in the work:

Table 4: Diffraction elastic constants for each sub-layer and substrate

Component	hkl	$S_1^{hkl} (* 10^{-6} MPa^{-1})$	$\frac{1}{2}S_2^{hkl}(* 10^{-6} MPa^{-1})$
K-Al ₂ O ₃	022	-0.683	3.51
	122	-0.689	3.53
	132	-0.703	3.57
α -Al ₂ O ₃	012/024	-0.685	3.36
	110	-0.557	2.96
Zr(C,N)	111	-0.45	2.785
	220	-0.44	2.755

Source: Eigenmann; Eshelby (1957); Kröner (1958); Macherauch (1996)

5.2.3 Crystallographic texture

To estimate if the coatings present a significant preferential orientation of growth and which would be this orientation, the texture coefficient (TC) was determined based on equation 18 (BARRET; MASSALSKI, 1980):

$$TC(hkl) = \frac{\frac{I(hkl)}{I_0(hkl)}}{\frac{1}{n}[\sum \frac{I(hkl)}{I_0(hkl)}]} * 100\% \quad \text{Eq. (18)}$$

Where $I(hkl)$ and $I_0(hkl)$ are the measured integrated intensities and the integrated intensities of a standard powder sample for the (hkl) reflection, respectively, and n is the number of reflections involved.

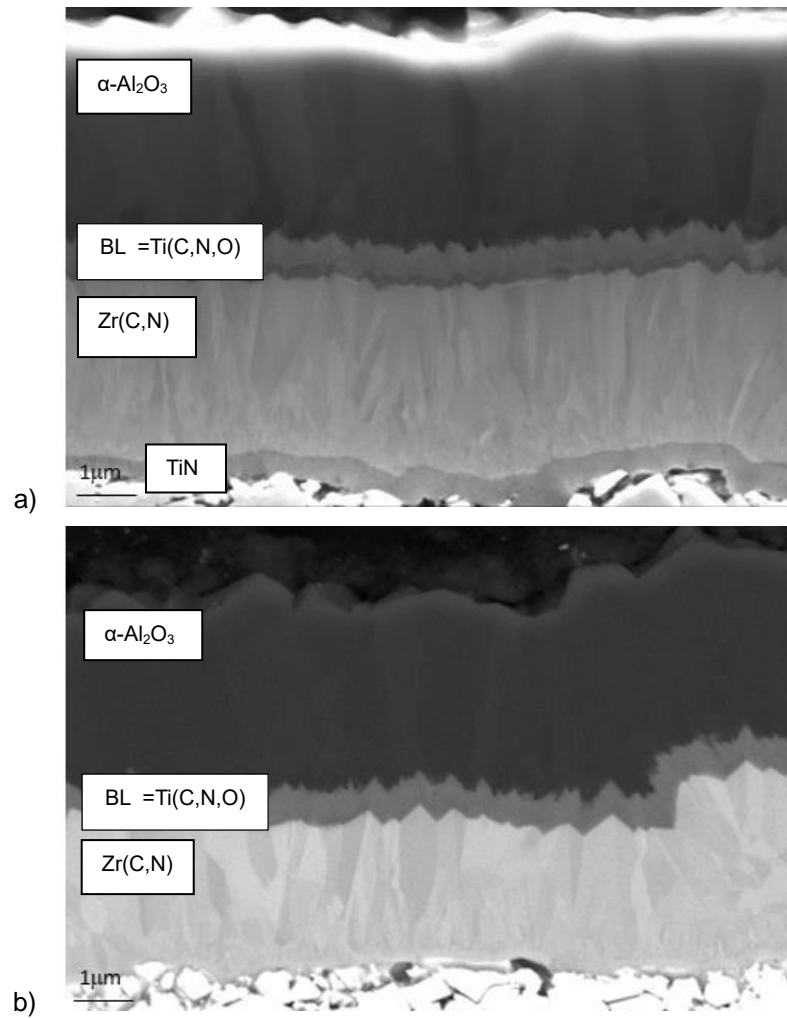
The crystallographic texture is a major issue in the stress analysis because if there is a high influence of the film texture (materials with a strong elastic anisotropy), non-linear d^{hkl} vs. $\sin^2\psi$ distribution will occur, thus invalidating the use of the $\sin^2\psi$ method.

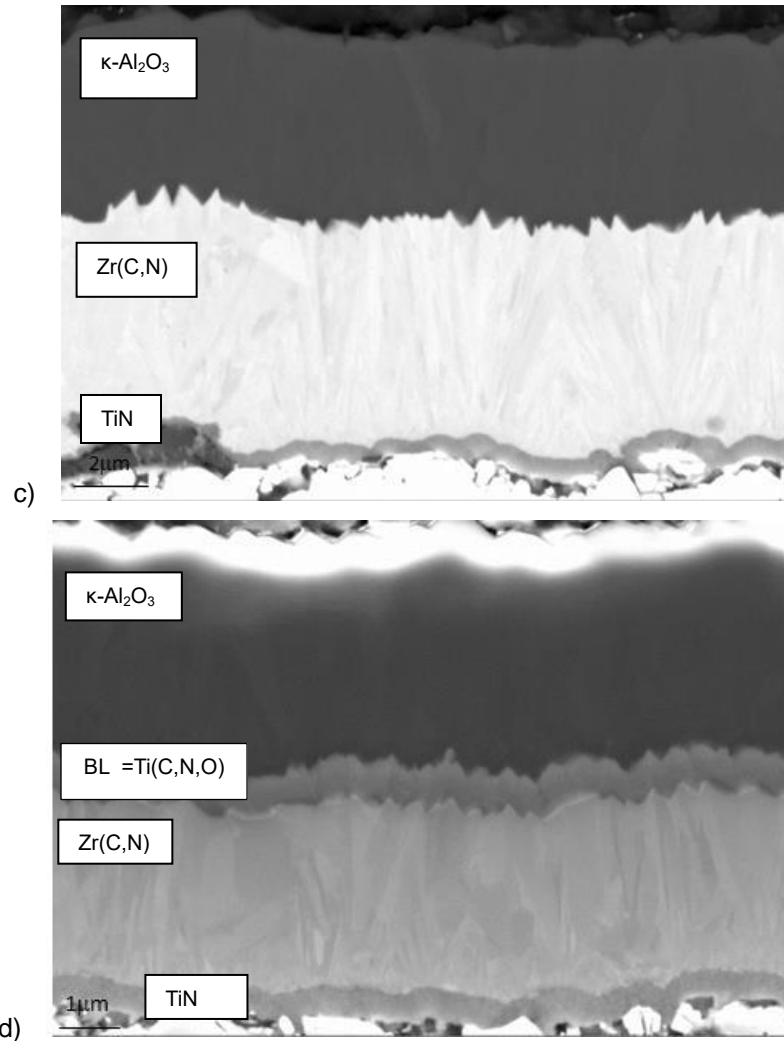
6 RESULTS AND DISCUSSION

6.1 Microstructural characterization

Fig. 14 shows SEM images for the Zr(C,N)-based system.

Fig. 14: SEM images for the Zr(C,N)-based system a) Zr(C,N)_ α b) Zr(C,N)_ α _b c) Zr(C,N)_k d) Zr(C,N)_k_BL





Source: The author

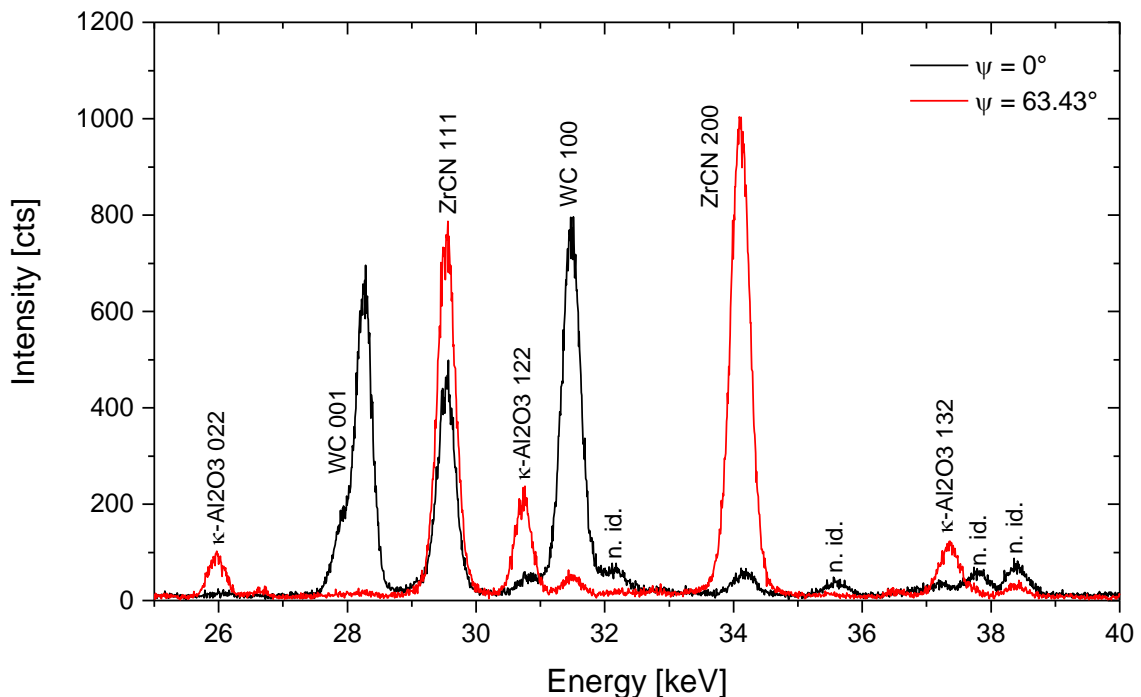
The thickness of the starting TiN layer is approximately $0,3 \mu\text{m}$ for the samples a), c) and d). For sample b) the starting ZrN layer is also $0,3 \mu\text{m}$ thick. The $\alpha\text{-Al}_2\text{O}_3$ and $\kappa\text{-Al}_2\text{O}_3$ layers are approximately $3,5 \mu\text{m}$ thick for all samples. The Ti(C,N,O) bonding layer for the images a) and d) is approximately $0.5 \mu\text{m}$ thick, whereas for the thickness of the Zr(C,N) layer was approximately $3,5 \mu\text{m}$. Columnar grain growth is observed in the Zr(C,N) layer. The microstructure of Zr(C,N) was investigated by El Azhari et al. (2018).

6.2 ED Diffraction

The XRD analyses were carried out using the strongest diffraction peaks of Zr(C,N), α -Al₂O₃ and κ -Al₂O₃. Since the Ti(C,N,O) bonding layers and the starting layer are rather thin, their diffraction lines are rather weak and may overlap with reflections from the Zr(C,N) layer. Hence the residual stresses of the starting and bonding layers were not analysed.

The ED diffraction patterns for the sample Zr(C,N)_k at $\psi = 0^\circ$ and 63.43° are shown in Fig. 15. The ED diffraction patterns exhibit diffraction lines which originate from the κ -Al₂O₃ and the Zr(C,N) layers as well as from the WC substrate beneath. For the κ -Al₂O₃ phase three diffraction lines could be used for the stress and texture analyses (022/122/132). Furthermore, some additional diffraction lines which we were not able to assign to any of the three components (these lines are denoted by *not identified* in Fig. 15) can be seen. Since these unidentified reflections become weaker and even vanish with increasing tilting angle ψ , it can be assumed that they originate from some unknown phase in the substrate, probably subcarbides of the type (Me,Co)_xC, fluorescence escape or Ge-drift peaks. Fig. 15 illustrates a diffractogram for the Zr(C,N)-based system.

Fig. 15: Diffractogram for a Zr(C,N)-based system.



Source: The author

6.3 Crystallographic texture of CVD layers

The TC of both the Zr(C,N) and the Al₂O₃ layers were obtained using Eq. 18. Tables 5 and 6 present the (*hkl*) planes with the highest texture coefficient for each layer. The TCs for Zr(C,N) vary between 1,1 and 3,76; showing that those layers are not heavily textured. The Al₂O₃ layers achieve a maximum TC of 5,16 and exhibit therefore a slightly stronger texture if compared to Zr(C,N). However, the texture of Al₂O₃ cannot be considered as strong or relevant, since for significant elastic anisotropy TCs above 10 are usually observed (ÅSTRAND et al, 2004; CHEN et al. 2006).

Tab. 5: (*hkl*) planes of maximum intensity for Zr(C,N)

Sample	(<i>hkl</i>) planes of maximum intensity Zr(C,N)	TC
Zr(C,N)_k	220	2,21
Zr(C,N)_α		3,76
Zr(C,N)_k_BL		2,98
Zr(C,N)_α_b		1,1

Source: The author

Tab. 6: (*hkl*) planes of maximum intensity for Al₂O₃

Sample	(<i>hkl</i>) planes of maximum intensity Al ₂ O ₃	TC
Zr(C,N)_k	013 (k)	4,75
Zr(C,N)_α	0012 (α)	5,01
Zr(C,N)_k_BL	013 (k)	2,98
Zr(C,N)_α_b	013 (k)	5,16

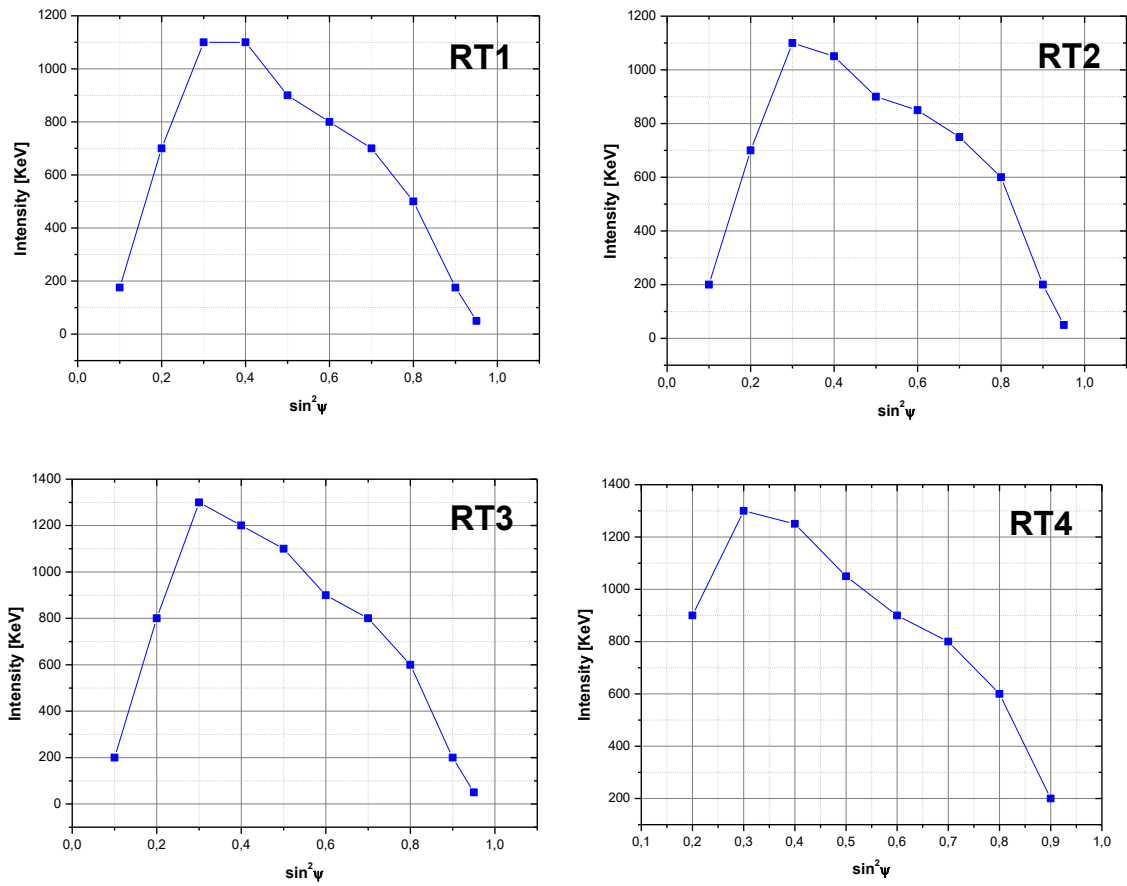
Source: The author

The crystallographic texture of the layers is not affected by the heating process, independently if blasting is applied or not. Sufficient diffracted intensity was observed at all ψ -tilts, also outside the intensity poles of texture, which ensures a good statistic for the linear regression procedure mentioned in the experimental procedure for the $\sin^2\psi$ -analysis.

Fig. 16 to 17 display a result the integrated diffraction intensities vs.

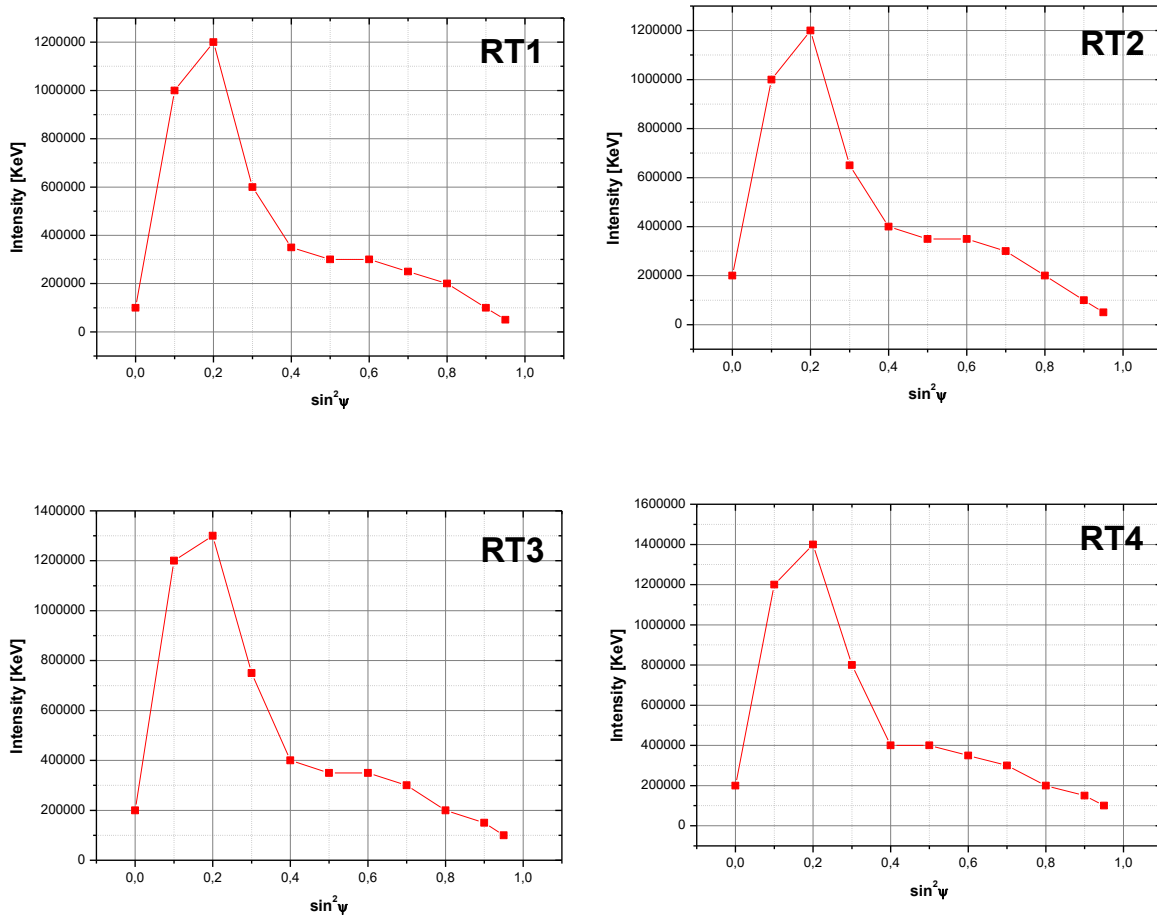
$\sin^2\psi$, for a sample of the Zr(C,N) system and another of the Al_2O_3 sub-layer. Texture does not influence the measure, because the shape of the intensity curve is the same before and after the heating. Sufficient intensity is available at all ψ -tilts of the samples.

Fig. 16: Integral line intensity for Al_2O_3 layer



Source: The author

Fig. 17: Integral line intensity for Zr(C,N) layer



Source: The author

6.4 Residual stresses

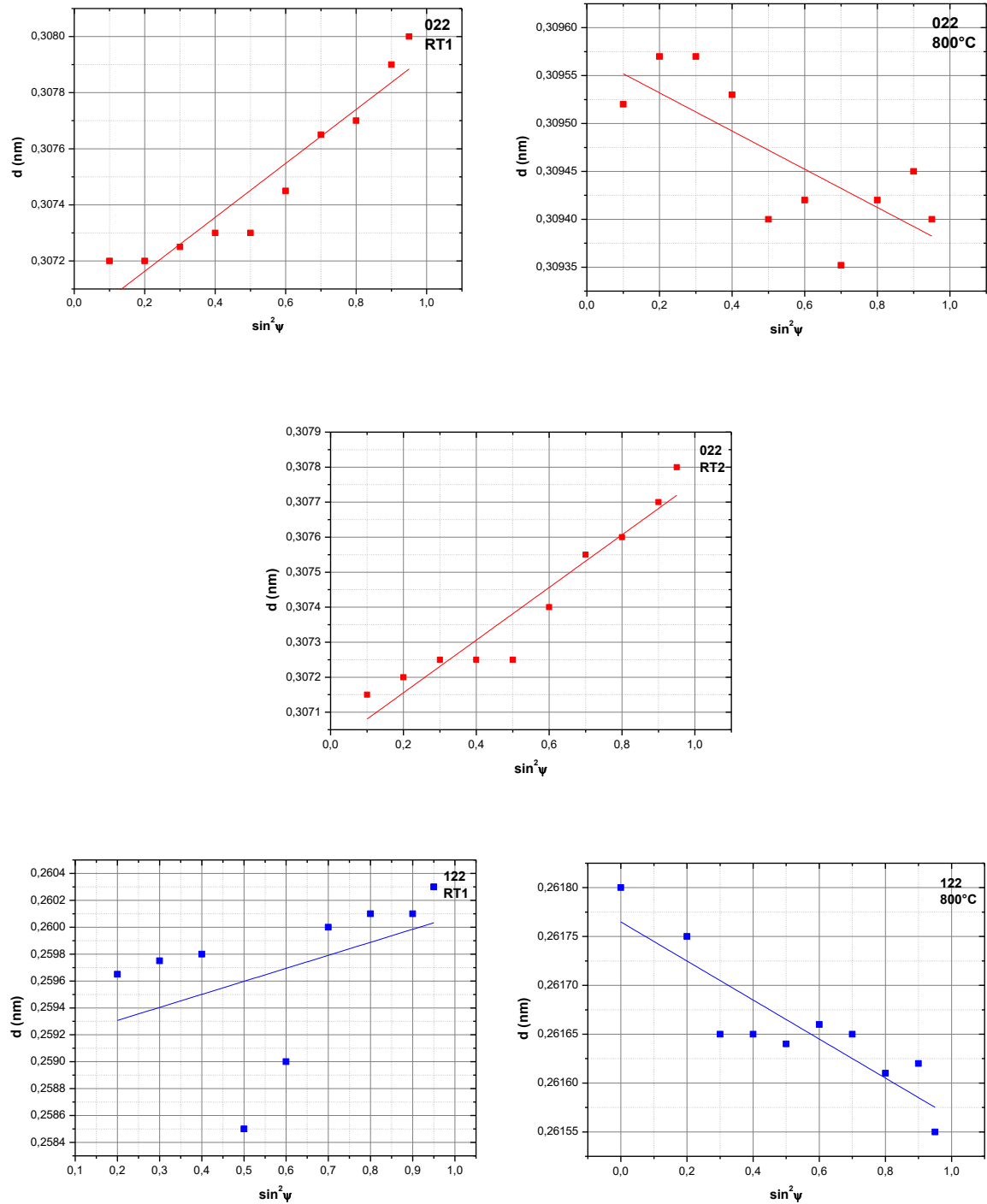
Using the $\sin^2\psi$ method it was possible to obtain representative results because the assumption underlying this method is approximately fulfilled: biaxial stress state, random or moderate texture and absence of steep stress gradients (almost linear $\sin^2\psi$ distributions).

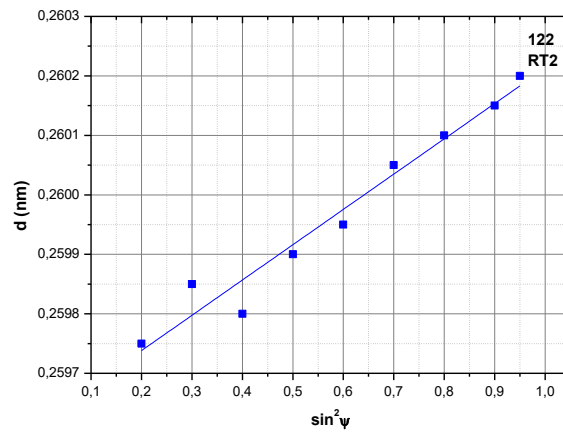
Fig. 18 presents the behaviour of d^{hkl} vs. $\sin^2\psi$ curves for the κ -Al₂O₃ layer for the 022 (red lines) and 122 planes (blue line) in Zr(C,N)_k sample.

The distributions of d^{hkl} vs. $\sin^2\psi$ appear linear and do not present systematic and continuous oscillations in general. Thus, the sample presented a strict linear distribution in the case of 022 (red line) and 122 (in blue) at the RT1 and RT2.

But at 800°C the reflection shows some non-systematic scattering about the regression lines, which may be a result of the low intensities of these lines.

Fig. 18: d^{hkl} vs. $\sin^2\psi$ curves for the Zr(C,N)_k sample of κ -Al₂O₃ layer for the 022 and 122 hkl planes



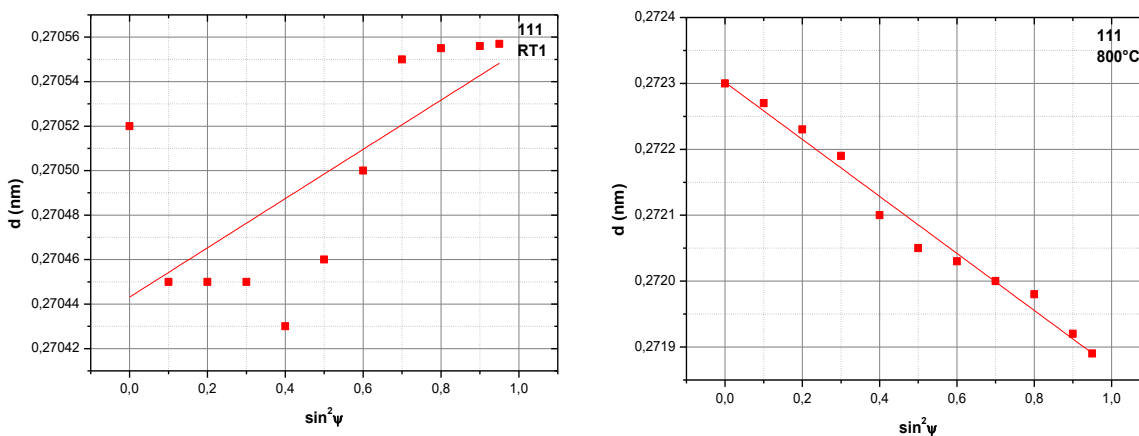


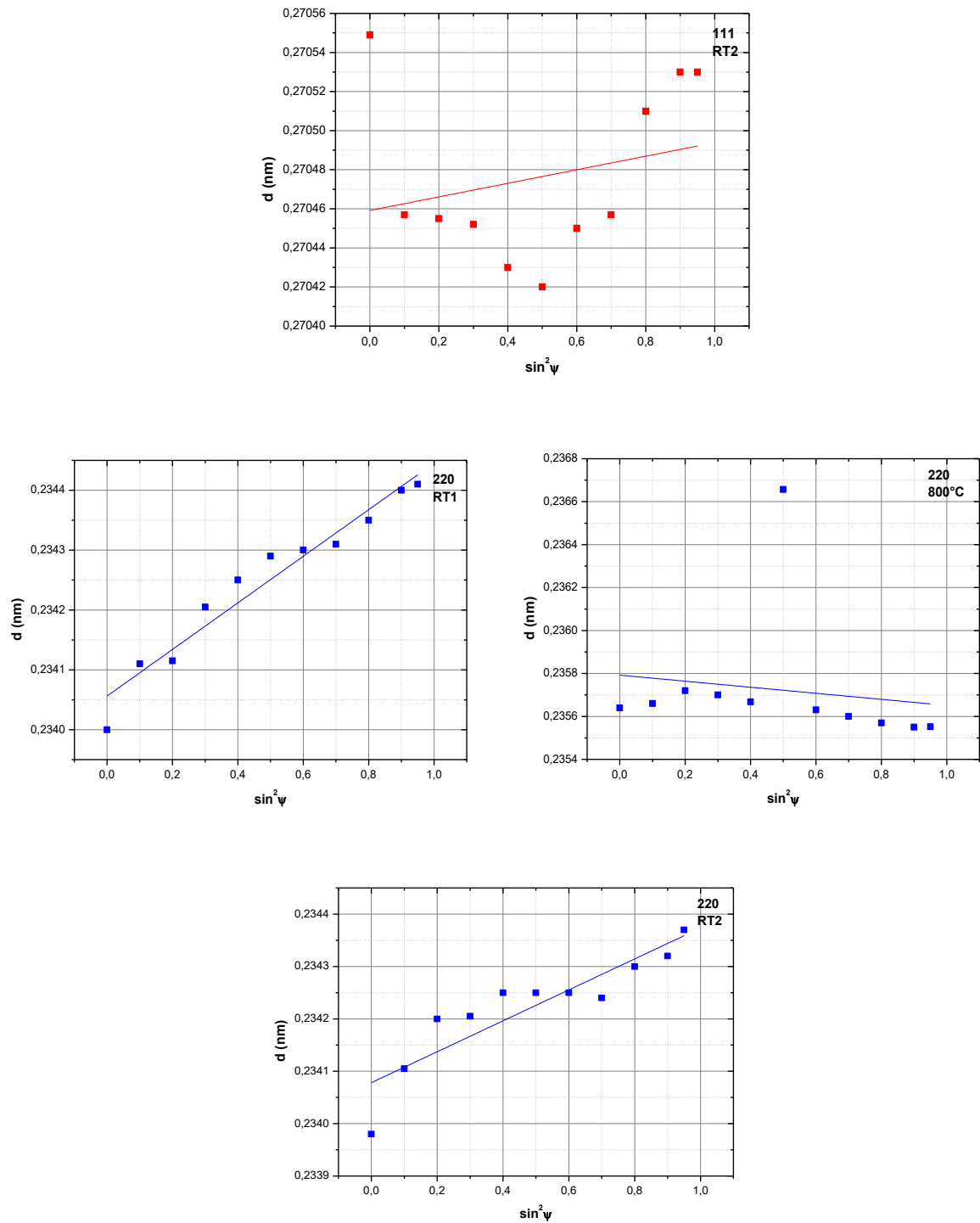
Source: The author

Fig. 19 shows the behaviour of d^{hkl} vs. $\sin^2\psi$ curves for the Zr(C,N) layer for the 111 (red lines) and 220 planes (blue line) in sample Zr(C,N)_k.

The distributions of d^{hkl} vs. $\sin^2\psi$ appear linear and do not present systematic and continuous oscillations. Thus, the sample presented a strict linear distribution in the case of 111 (in red) at the 800°C but not at RT. At RT, the reflection shows some non-systematic scattering about the regression line, which may be a result of the low intensities of these lines. In the case of the 220 reflexion (in blue) the sample presented a strict linear distribution at all temperatures.

Fig. 19: d^{hkl} vs. $\sin^2\psi$ curves for the Zr(C,N)_k sample of Zr(C,N) layer for the 111 and 222 hkl planes



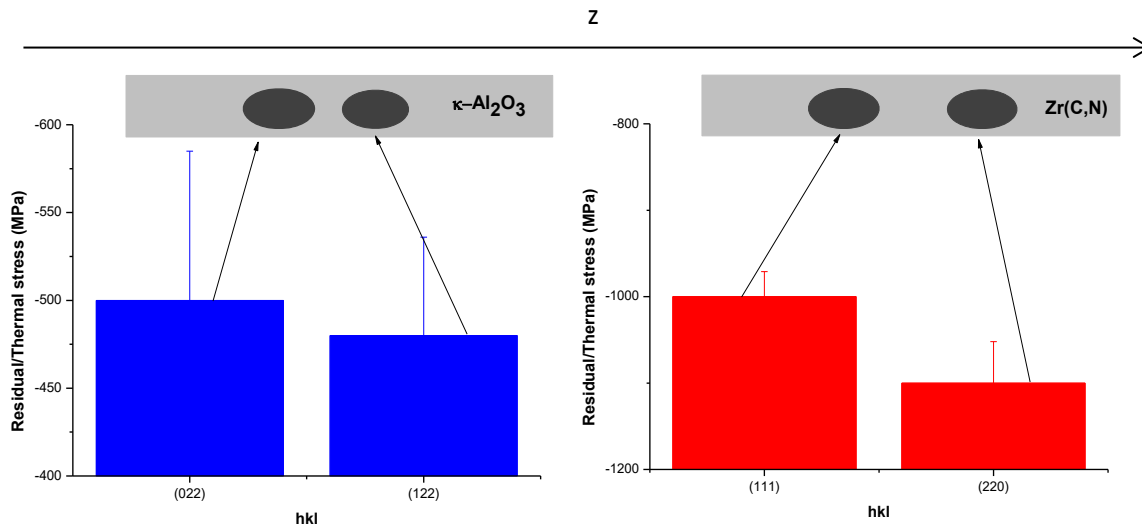


Source: The author

In the present case, we do not have compositional gradients within the sub-layers. Thus, the depth results of the residual/thermal stresses do not depend on the variations of elastic and thermal material properties of the thin film, as well as on the changes of the strain-free d_0 -spacing with the depth into the sub-layers. Fig. 20

shows that the stresses for different (hkl) lattice planes are not significantly different. This indicates that an average value over the multiplicity of each (hkl) plane is the most adequate choice to determine representative stress values for each sub-layer. This is the procedure adopted to quantify the residual stresses for all layers in this work.

Figure 20: Example of data obtained of residual stress for different (hkl) planes, i.e, different depths within the sub-layers



Source: The author

Table 7 shows an example of how the residual stress values were obtained for the Zr(C,N) layer in the Zr(C,N)_k sample. The average stress values were calculated by removing the values where the error was of the same magnitude or higher than the calculated stress value. Values for those plots where the linear regression was not possible due to a broad scatter of d^{hkl} vs. $\sin^2\psi$ were also eliminated of the calculation.

Table 7: Results of residual stresses for the 111 and 220 planes in the Zr(C,N) layer

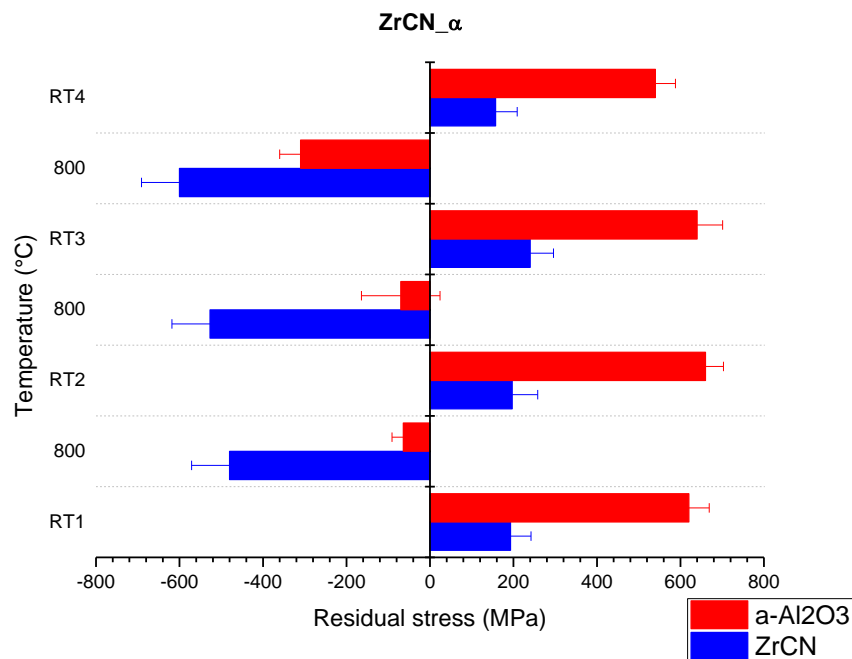
Zr(C,N)_k			
	RT1	800	RT2
111	800 ± 92	-100 ± 93	700 ± 88
220	750 ± 51	-150 ± 53	750 ± 36
Average	775 ± 72	-125 ± 73	725 ± 62

Source: The author

6.4.1 Effect of blasting in Zr(C,N)/ α -Al₂O₃ layers at RT/800/RT thermal cycle

The first evaluation focus on both the thermal cycling behaviour for three thermal cycles (RT/800/RT) in the Zr(C,N)/ α -Al₂O₃ system, as well as the effect of alumina top-blasting on this behaviour. The results for sample Zr(C,N) _{α} are shown in Fig. 21.

Figure 21: Residual stresses for sample Zr(C,N) _{α} in as-coated condition



Source: The author

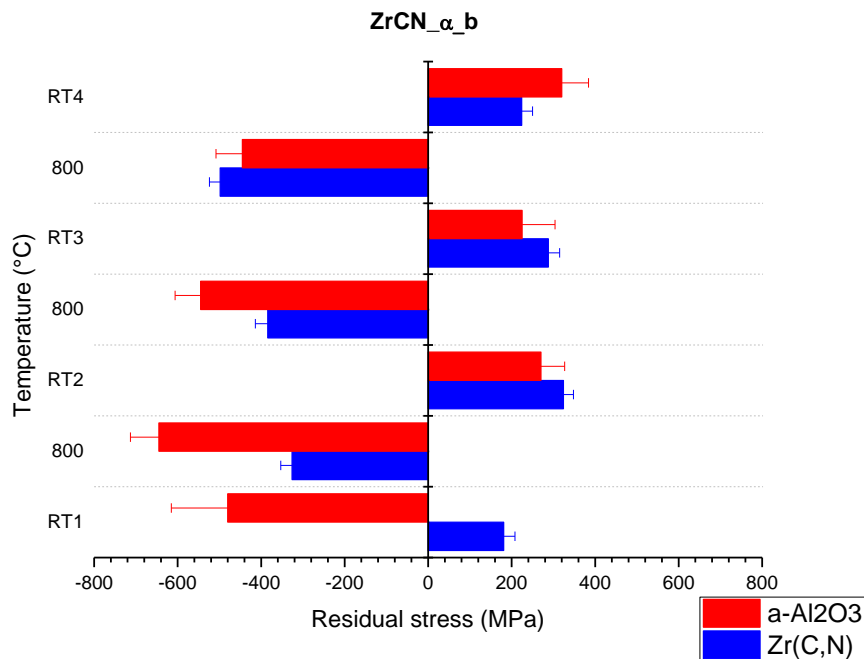
Fig. 21 shows the results of the in-situ stress evolution during three thermal cycles for the Zr(C,N)/ α -Al₂O₃ system in the as-coated condition (sample Zr(C,N) _{α}). In the α -Al₂O₃ (in red) residual stresses have magnitude of ~ 600-700 MPa, being tensile stresses at all RT in the three repetitions. The high temperature measurements at 800°C shows that the α -Al₂O₃ layer develops compressive stresses during the heating reaching approximately -150MPa. In the final heating at 800°C, residual stresses evolve to compressive stresses of -300MPa, which is above the value for the first and second heat step. The similar values of residual stresses during all heating and cooling steps indicate a kind of thermal stress cycling behaviour dependent on the temperature values.

For the Zr(C,N) layer a similar residual stress behaviour as for the α -Al₂O₃

thin film was observed, however, with different stress magnitudes. At all RT a tensile stress value of approximately 200 MPa was calculated and by increasing the temperature to 800°C compressive stresses of -450 MPa, -500 MPa and -600 MPa were observed respectively in each of the three high temperature measurements. Interestingly the residual stresses for the layers at the last 800°C-RT4 present values higher than the first and second cycle in compressive behaviour. However it can be concluded that the as-deposited coating systems behaves almost elastic and the residual stresses changes associated to temperature changes.

The results for the sample Zr(C,N)_ α _b are shown in Fig. 22.

Figure 22: Residual stresses for the sample Zr(C,N)_ α _b



Source: The author

Fig. 22 presents the results for the residual stresses for the Zr(C,N)_ α _b sample. The main difference with the previous sample is the post-treatment process (top-blasting) carried out after CVD coating. In the α -Al₂O₃ layer, residual stresses at RT1 has a compressive nature with a magnitude of approximately -500 MPa. At all RT in the subsequent cycles tensile stresses with values varying between 150 MPa and 350 MPa. At all 800°C in the three cycles the stress evolves to compressive stresses reaching magnitude of -650 MPa to -500 MPa.

For the Zr(C,N) layer a behaviour compared to the α -Al₂O₃ was observed,

except for RT1 condition. The Zr(C,N) layer presents tensile residual stresses at RT1 that evolve to compressive at 800°C. In the subsequent cycles the residual stress values oscillates between tensile (200 MPa ~ 300 MPa) and compressive (-300 MPa, -400 MPa and -500 MPa).

The main observation of this study is that the blasting process directly influences the stress behaviour of the top oxide layer (α -Al₂O₃). This behaviour can be understood by comparing the residual stress condition at RT1 in Fig 21. (as coated) and Fig. 22 (top blasted). After the first heat cycle the compressive stresses evolve to tensile in the top-blasted sample. The residual stresses at RT2 are of the same magnitude and value for both as-coated and top-blasted samples. In the subsequent cycles both systems behave similar in terms of residual stress evolution. Interestingly the residual stress evolution of the carbonitride layer is not influenced by the top-blasting process, indicating that the top-blasting effect is confined to the α -Al₂O₃ layer. The Zr(C,N) residual stress evolution is indeed alternating with the temperature fluctuations presenting a cycling behaviour.

Recently works in blasting processes for CVD coatings have confirmed that the introduction of compressive stresses in the α -Al₂O₃ layer by top-blasting is associated to generation of defects in the layer. Upon heating these defects are annihilated and the system evolves to tensile stresses due to relaxation. For the carbonitride layers no structural modification is achieved by the top-blasting process, therefore no changes of residual stresses are observed by mechanical impact, since the energy of the top-blasting process is consumed in the generation of defects in the α -Al₂O₃ top-layer (GARCÍA et al, 2019). In a recent work the author also described that the level of residual stresses in the α -Al₂O₃ top-layer can be adjusted by varying the blasting conditions (parameters such as pressure and impact particle material), and even the residual stress of the cemented carbide (WC phase) can reach compressive state by intensive shot-peening with larger particles (MORENO et al, 2019). Another work indicates that shot-peening (high energy blasting) may affect both the residual stress of the carbonitride layer and hard metal (FAKSA, et al. 2019).

It can be concluded that the results of this investigation agrees with previous studies on Ti(C,N)/ α -Al₂O₃ systems [GARCIA 2017]; indicating that the presence of the Zr(C,N) layer replacing the Ti(C,N) does not have a strong effect on

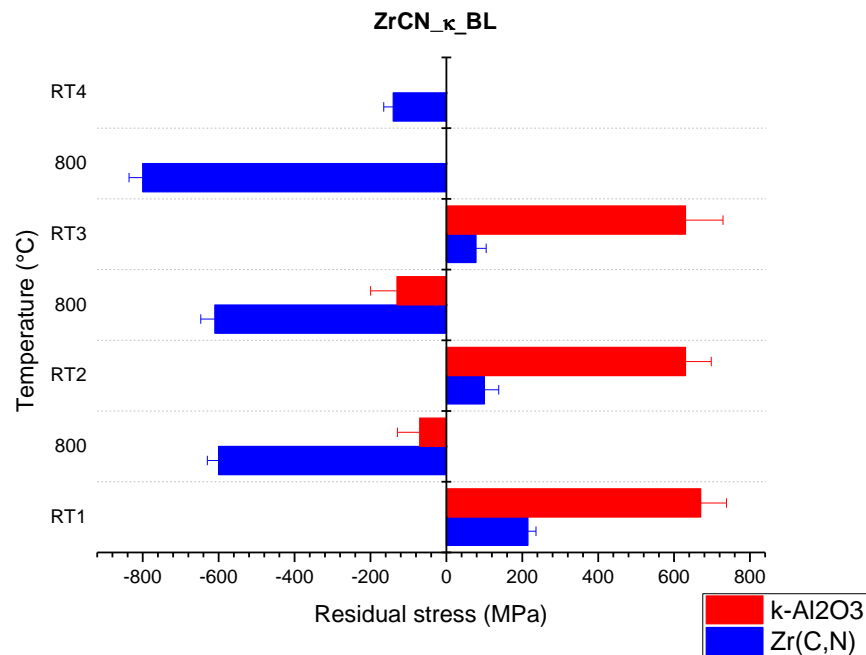
the residual stress behaviour of the α -Al₂O₃ layer in the as-coated and top-blasted condition.

6.4.2 Effect of Ti(C,N,O) bonding layer in Zr(C,N)/ κ -Al₂O₃ layers at RT/800/RT thermal cycle

In this chapter the α -Al₂O₃ is replaced by κ -Al₂O₃ in the Zr(C,N)-based system. Two type of samples were produced, one containing a bonding interlayer similar to the one used in α -Al₂O₃ systems consisting of a Ti(C,N,O) phase. The concept of the bonding layer is to produce a graded interface between the carbonitride layer and the oxide layer by incorporating oxygen to the carbonitride to favour the nucleation and growth of the Al₂O₃ layer. This transition layer has proven to be effective in terms of control of crystallite size, texture and crystal orientation in Al₂O₃ layers. The systems are compared in as-coated condition without any post-treatment process.

Fig. 23 shows the residual stress results for the Zr(C,N)_ κ _BL sample.

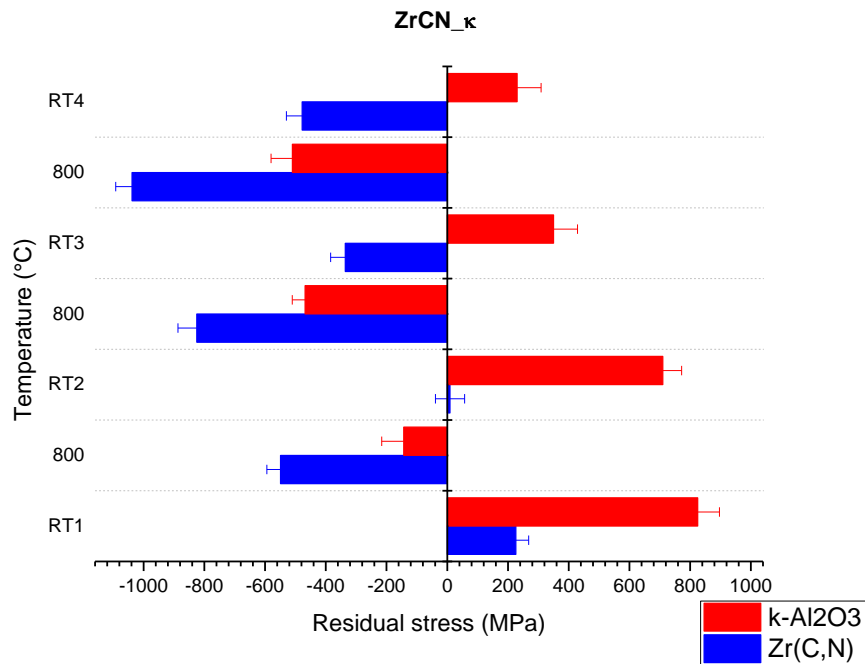
Fig. 23: Residual stresses for the sample Zr(C,N)_k_BL



Source: The author

Fig. 23 exhibits the results of the residual stress evolution during three thermal cycles for the Zr(C,N)/k-Al₂O₃ system containing a bonding layer in the as-coated condition (sample Zr(C,N)_k_BL). In the k-Al₂O₃ (in red) residual stresses have a magnitude of 600-650 MPa (tensile stresses) at RT. At high temperature 800°C, the residual stresses develop in compressive stresses reaching approximately -150 MPa. The similar values of residual stresses during the heating up and cooling down steps indicates a kind of thermal stress cycling behaviour dependent on the temperature values. Note: the reflexion of the k-Al₂O₃ layer were no available for evaluation in the last cycle due to problems in the data collection, for this reason they are omitted in this graph and evaluation.

A similar residual stress cycling behaviour as for k-Al₂O₃ was observed for the Zr(C,N) layer in this system. At RT a tensile stress value varying between 100-200 MPa was observed and by increasing the temperature to 800°C compressive stresses of -600-800 MPa were observed. Fig. 24 shows the residual stress results for the Zr(C,N)_k without bonding layer sample.

Fig. 24: Residual stresses for the sample Zr(C,N)_κ (no BL layer)

Source: The author

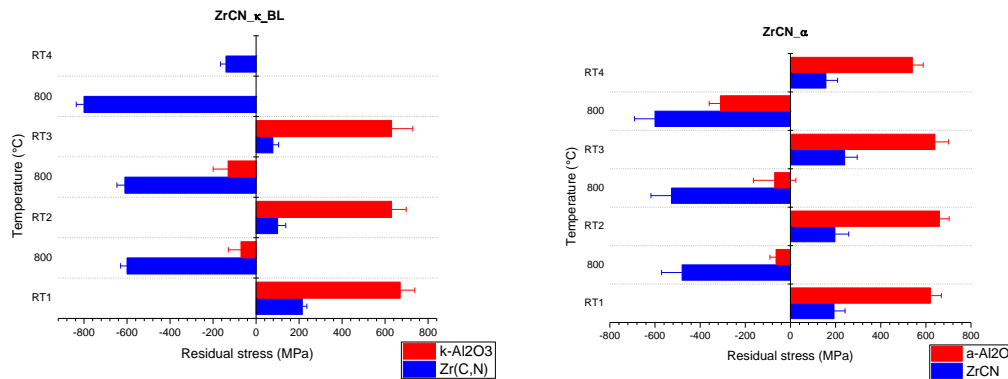
Fig. 24 shows the results of the in-situ stress evolution during three thermal cycles for the Zr(C,N)/ κ -Al₂O₃ system without Ti(C,N,O) layer in the as-coated condition. In the κ -Al₂O₃ layer (in red) residual stresses have tensile residual stresses (magnitude of 800 MPa, 700 MPa, 400 MPa and 200 MPa at the RT1, RT2, RT3 and RT4 respectively). In the high temperature measurements (800°C) the residual stresses of the κ -Al₂O₃ layer evolve to compressive stresses reaching approximately -100MPa. In the second and third heat step it was observed a compressive stress of -500MPa, which is higher than the value for the first heat step. In this case it is also possible to correlate the stress values during all heating/cooling steps with a kind of thermal stress cycling behaviour dependent on the temperature values.

For the Zr(C,N) layer a different behaviour compared to the κ -Al₂O₃ layer was observed. At RT1 a tensile stress value of approximately 200 MPa was obtained. For the immediate next RT, a compressive behaviour was observed, which remained compressive in the following cycles, the values ranging between -75 MPa and -900 MPa for different temperature conditions.

When comparing both systems with and without bonding layer a remarkable difference is noticed for the residual stress behavior of the Zr(C,N) layer. In the system with Ti(C,N,O) bonding layer, both the k-Al₂O₃ and the Zr(C,N) layer follows the same cycling behaviour in terms of temperature fluctuations (ranging from tensile at room temperature to compressive at high temperatures). However when the bonding layer is omitted then the k-Al₂O₃ and the Zr(C,N) do not follow the same trend in cycling response to temperature. The k-Al₂O₃ shows the expected cycling behaviour of residual stresses; contrary, the Zr(C,N) layer changes the residual stress from tensile to compressive in the first heating and remains compressive in the following temperature fluctuations. This is an indication that the bonding layer contributes to a better matching in thermal stresses between the layers, and that by avoiding the bonding layer, both layers present independent residual stresses. Despite the Zr(C,N) layer presents compressive stresses during the entire thermal cycles, the absolute values are lower at RT conditions (see RT2, RT3, RT4). In the case of the system with a bonding layer, both layers behaves as a bonded composite and this independent behavior in terms of expansion/contraction is limited. It is known that the presence of a bounding layer, Ti(C,N,O) favours the nucleation of k-Al₂O₃ and gives a better adhesion between the oxide and carbonitride layer (HALVARSSON; TRANCIK; RUPPI 2006).

6.4.3 Residual stress behaviour for Zr(C,N)/k-Al₂O₃ and Zr(C,N)/α-Al₂O₃ layers with bonding layers at RT/800/RT thermal cycles

The final comparison focus strictly on the comparison of the different Al₂O₃ types in similar systems containing Zr(C,N) and Ti(C,N,O) bonding layers in the as-coated condition. Comparisons in the top-blasted condition are not possible, since the metastable k-Al₂O₃ does not have enough strength to resist deformation by mechanical impact at high energies. As shown in the previous chapter, comparisons without bonding layer are also not possible, in particular for the Zr(C,N) residual stress behavior at cycling temperature conditions. Fig. 25 shows the residual stress comparison for the samples Zr(C,N)_α and Zr(C,N)_k_BL sample.

Figure 25: Residual stresses for the sample Zr(C,N)_α and Zr(C,N)_k_BL

Source: The author

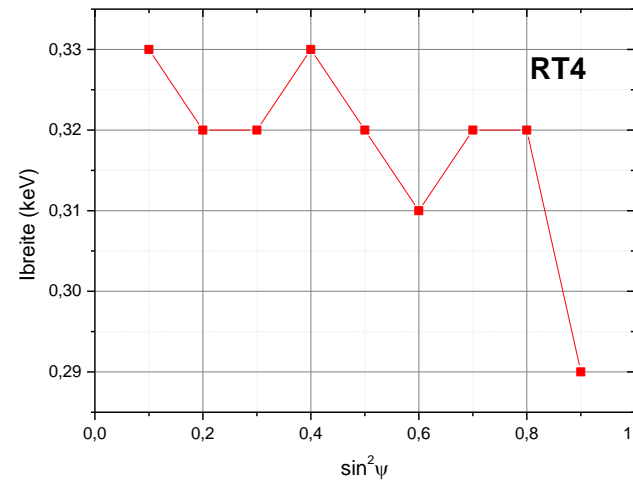
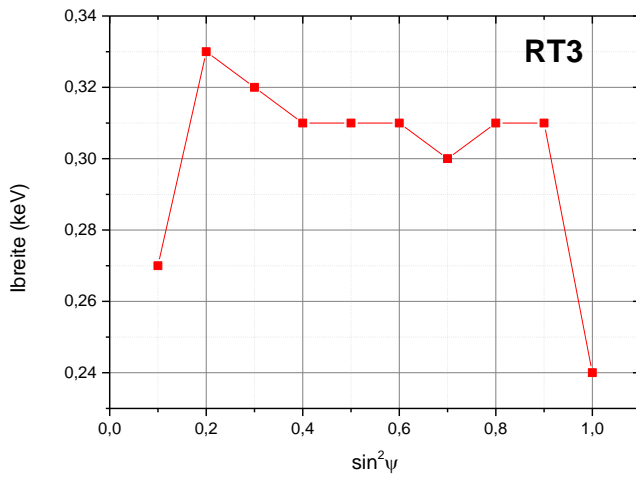
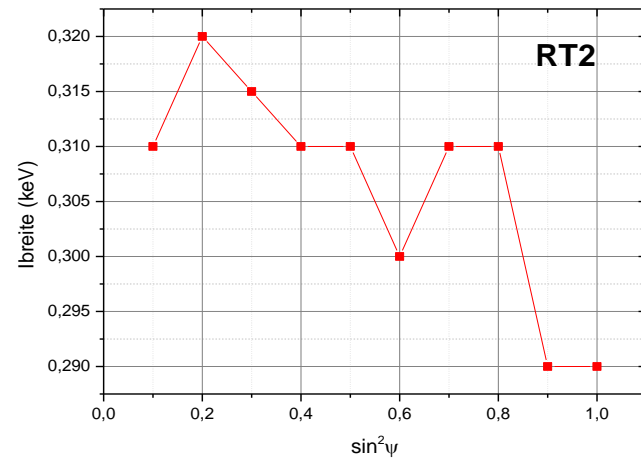
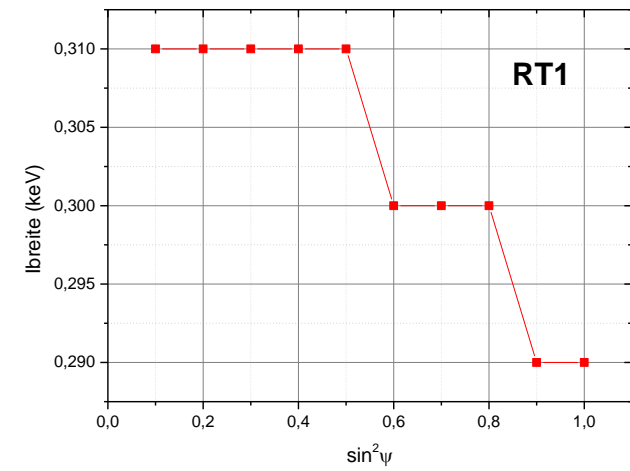
As can be seen in Fig. 25 the in-situ stress evolution during thermal cycle for both systems is very similar. The absolute values for the Zr(C,N) layers are almost of the same intensity. One could argue that the Zr(C,N) layer presents a slightly more compressive behaviour in the k-Al₂O₃ system, but the values are considered to have statistical errors and the number of samples and measurements have been limited. Based on these results it can be concluded that the type of Al₂O₃ does not have an effect on the residual stresses response of this carbonitride/oxide system. The observed differences in absolute values can be related to the crystalline structure, degree of plasticity, pore density, grain size of the layers that can influence in the stresses as reported in Barbatti et al (2009).

6.4.4 Effect of the heating in the microstructure of each sub-layer

It is possible to relate the diffraction line broadening with the material microstructure before and after heating. In order to evaluate an average domain size and microstrain from the integral line width, measurements on standard powders have to be performed to quantify and to take instrumental broadening into account (Genzel et al, 2017). Although this was not carried out in the present case, the *relative comparison* of the integral line width *before* and *after* heating reveals valuable information on microstructural changes such as annealing of intrinsic defects.

Fig. 26 presents an example for the Al₂O₃ layer.

Fig. 26: Integral line width for the Al₂O₃ layer



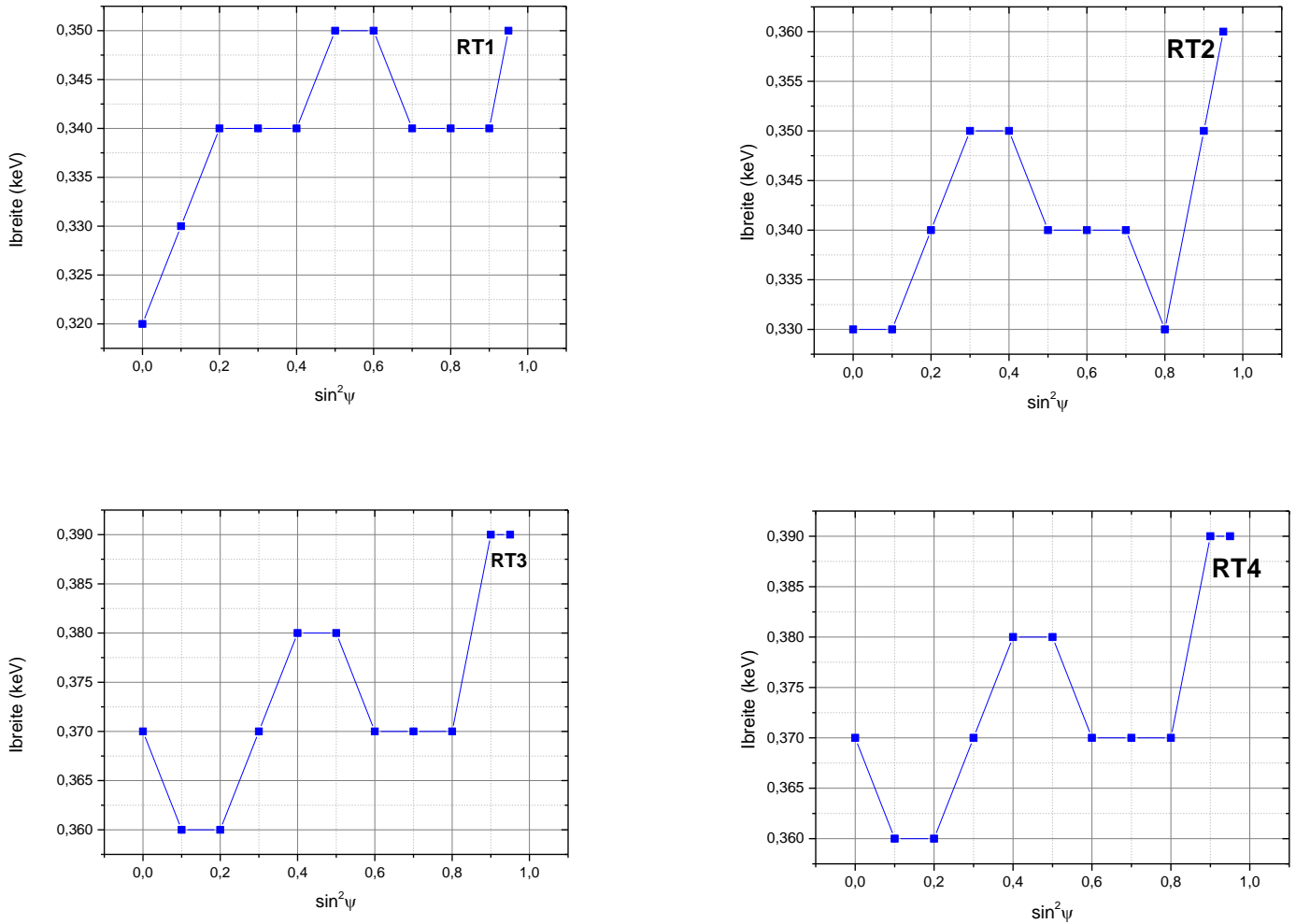
Source: The author

It is possible to observe that, the alumina layer did not presented differences in the integral diffraction line width, that indicates that the heating process did not affected the microstructure and texture of this layer.

The heating process does not affect the texture of the alumina layer.

Fig. 27 displays an example of the evolution of the integral breadth with the ψ -tilt for the Zr(C,N) layer.

Fig. 27: Integral line width for the Zr(C,N) layer



Source: The author

It is possible to observe that, the alumina layer presented a slow increase in the integral diffraction line width, that indicates the formation of intrinsic lattice defects. The heating process does not affect the texture of the carbonitride layer.

6.4.5 Theoretical residual stresses of Zr(C,N), κ -Al₂O₃ and α -Al₂O₃

It is important to consider in the discussion the theoretical values of the thermal stresses (originated from temperature fluctuations) for the layers investigated

in this work. Below we have one approach to calculate those values:

If a multi-layer system is considered, the equation can be adapted from (MCGINNIS et al. 1999) as follows:

$$\sigma = \frac{E_L}{(1-\nu_L)} * (CTE_M - CTE_L) * (T - T_{max}) \quad \text{Eq. (19)}$$

Where σ is the stress, E_L is the Young 'modulus of the layer, ν_L is the poisson coefficient of the layer, T is values of temperature that the samples varied and T_{max} is the maximum temperature of the deposition (1050° C), CTE_M is an average CTE for the substrate and the sub-layers in the case, i.e. $CTE_M = CTE_S * \left(\frac{h_S}{h_T}\right) + CTE_{LN} \left(\frac{h_{LN}}{h_T}\right)$ TEC_S is the thermal expansion coefficient of the substrate, CTE_{LN} is the thermal expansion coefficient of the layer, h_S is the length of the substrate, h_{LN} is the thickness of the layer (N = 1, 2, 3 ... represents the number of layers in the system and is the same N of the CTE), and h_T is the sum of h_S and h_{LN} .

Having these relations it is possible to evaluate the theoretical values of the thermal stresses for the Al₂O₃, Ti(C,N) and Zr(C,N) layers. Table 8 presents the elastic and thermal properties used to calculate the stresses.

Table 8: Elastic, thermal properties and theoretical residual stresses for substrate and coating layers

Substrate/coating layer	E [GPa]	ν	TEC [10 ⁻⁶ /K]	σ (MPa) at RT	σ (MPa) at 800°C
WC	707	0,22	5,2	-	-
α -Al ₂ O ₃	440	0,21	7	1027,6	250,6
k-Al ₂ O ₃	344	0,24	6,15	440,8	107,5
Zr(C,N)	410	0,21	6,95	930,9	227

Source: Accuratus (2013); Rупpi et al. (2007); Friedrich et al. (1997); Kral et al. (1998)

The thickness of the WC substrate (h_S) was assumed to be 5000 μm . The thickness of the Al₂O₃ and Zr(C,N) were considered to be 4 μm , obtained in the tables of the experimental part.

These differences between theoretical and experimental residual stresses values can be explained by the relaxation of stresses due to microcracking during the cooling down of the CVD process.

7 CONCLUSIONS

The residual stress evolution in Zr(C,N)/ α -Al₂O₃ and Zr(C,N)/ κ -Al₂O₃ CVD layers during thermal cycling has been investigated. As a result of this work following conclusions can be summarized:

- A cycling behaviour of residual stress evolution was observed for the systems studied in Zr(C,N)-based. The cycling response is dependent on the temperature.
- The blasting process can introduce compressive stresses in the α -Al₂O₃ layer. The effect is confined to this top-layer and it does not reach the Zr(C,N) layer.
- The presence of different phases of Al₂O₃ in the multilayer system does not affect the residual stresses in the Zr(C,N) layer.
- The κ -Al₂O₃ layer presents slightly lower tensile stresses compared to the α -Al₂O₃ stresses results, that can be related to the differences between grain size, porosity, plasticity and structure of the coating.
- The presence of a Ti(C,N,O) bonding layer influences the residual stresses of the Zr(C,N) layer. For systems without bonding layer, the Zr(C,N) layer presents compressive stresses in the entire cycling conditions investigated. This behaviour differs from the Al₂O₃ response, indicating that both layers behave independently during the thermal fluctuations.
- For systems with Ti(C,N,O) bonding layer, both the Zr(C,N) and the Al₂O₃ layers present similar cycling response to thermal changes, indicating that the bonding layer not only enhance the adhesion between the layers but also contributes to matching expansion and contraction of the layers in the presence of

temperature variations.

- The integral line width of the layers shows that the heating process does not affect the texture of the layers.
- The theoretical residual stresses results indicate that exist a large difference between the these values and the experimental results. This can be understood by the relaxation of stresses due to microcracking during the cooling down of the CVD process.

REFERENCES

ACCURATUS, Aluminum Oxide, Al₂O₃ Ceramic Properties, 2013. Available in: <http://accuratus.com/alumox.html> Accessed in: 29 may 2019.

ADNAN, M. et al. "Fuzzy logic for modeling machining process: a review." **Artificial Intelligence Review** 43.3 p.345-379, 2015

ÅSTRAND, M. et al. PVD-Al₂O₃-coated cemented carbide cutting tools. **Surface and Coatings Technology** v.188, p. 186-192, 2004

BACZMANSKI et al. **Models of plastic deformation used for residual stress measurements**, Zeitschrift fur Metallkunde, v. 86, n. 7, p. 507-511, 1995

BARBATTI, C. et al. Influence of micro-blasting on the microstructure and residual stresses of CVD α -Al₂O₃ coatings. **Surface and Coatings Technology**, v. 203, n. 24, p. 3708-3717, 2009

BARRET, C. S.; MASSALSKI, T. B. **Structure of metals**. Oxford: Pergamon, 1980

BARTOSIK, M.; PITONAK, R.; KECKES, J. In Situ High Temperature X-Ray Diffraction Reveals Residual Stress Depth-Profiles in Blasted TiN Hard Coatings. **Advanced Engineering Materials**, v.138 p. 705-711, 2011

BHATIA, S.; PANDEY, P.; SHAN, H. Thermal cracking of carbide tools during intermittent cutting. **Wear**, v. 51, n. 2, p. 201-211, 1978

BHATIA, S.; PANDEY, P.; SHAN, H. The thermal condition of the tool cutting edge in intermittent cutting. **Wear**, v. 61 n. 1, p. 21-30, 1980

BOUZAKIS, K .D. et al. Effect on PVD coated cemented carbide inserts cutting performance of micro-blasting and lapping of their substrates. **Surface and Coatings Technology**, v.200, n.1, p.128-132, 2005

CAMPOS, M.F.; MACHADO, R.; HIRSCH, T. Tensões residuais em aços avaliadas por difração de raio-X: diferença entre micro e macro tensões residuais. In: WORKSHOP SOBRE TEXTURA, 3., 2006, São Paulo. **Anais...** São Paulo: CNPq/IPT/IPEN, p.115-131, 2006

CHEN, Li et al. Influence of pulse frequency on the microstructure and wear resistance of electrodeposited Ni–Al₂O₃ composite coatings. **Surface and Coatings Technology**, v. 201, n. 3, p. 599-605, 2006

EIGENMANN, B.; MACHERAUCH, E. Röntgenographische untersuchung von spannungszuständen in werkstoffen. Teil III. Fortsetzung matwiss. und werkstoffen. Heft 3/1995, S.148-160 und heft 4/1995, S.199-216. **Materialwissenschaft und Werkstofftechnik**, v.27, n.9, p.426 – 437, 1996

EL AZHARI, I. et al. Investigations on micro-mechanical properties of polycrystalline Ti(C,N) and Zr(C,N) coatings. **Acta Materialia**, v.149, p. 364-376, 2018

ERICSSON, T. Residual stresses caused by thermal and thermochemical surface treatments. **Advances in Surface Treatments**, v. 87128, p. 87-113, 2014

ESHELBY, J.D. The Determination of the elastic field of on ellipsoidal inclusion, and related problems. **Proceedings of the Royal Society A: mathematical, physical and engineering sciences**, v.241, n.1226, p.376-396, 1957

FAKSA, L. et al. Effect of shot peening on residual stresses and crack closure in CVD coated hard metal cutting inserts. **International Journal of Refractory Metals and Hard Materials**, 2019

FALLQVIST, M.; OLSSON, M.; RUPPI, S. Abrasive wear of multilayer κ -Al₂O₃-Ti(C,N) CVD coatings on cemented carbide. **Wear**, v. 263, n.1-6, p.74-80, 2007

GARCÍA J. Personal communication, 2019

GARCÍA, J., et al. Cemented carbide microstructures: a review. **International Journal of Refractory Metals and Hard Materials**, 2018

GARCÍA, J. et al. **Design of coated cemented carbides with improved crack resistance**. In: PLANSEE SEMINAR, 19., 2017, Reutte. Proceedings... Reutte: Plansee Group, 2017

GARCÍA, J. **Development of Wear Resistant Coatings for Cutting Tools**. In: World PM2016 – SIS 90 Years of Cemented Carbide – Past, present and future, Hamburg, 2016

_____. In-Situ high temperature stress analysis of Ti(C,N) coatings on functionally graded carbides by energy dispersive synchrotron X-ray diffraction. **International Journal of Refractory Metals and Hard Materials**, v.56, p.27–34, 2015a

_____. 3D-FIB characterization of wear in WC-Co coated composites. **Materials Science Forum**. v. 825-26, p. 995-1000, 2015b

_____. The Role of cemented carbide functionally graded outer-layers on the wear performance of coated cutting tools. **International Journal of Refractory Metals and Hard Materials**, v.36, p.52-59, 2013

_____. Design and characterization of novel wear resistant multilayer CVD coatings with improved adhesion between Al₂O₃ and Ti(C,N)". **Advanced Engineering Materials**, v.12, n.9, p.929-934, 2010

_____. **Process Development and scale up of cemented carbide production in Scale-up in Metallurgy** M. Lackner (Ed.), Ch. 9, p. 235-265 Verlag ProcessEng Eng GmbH, 2010

GENZEL C. et al. **Internal report** In-Situ high temperature stress analysis on coated

cutting tools by energy-dispersive diffraction performed at the EDDI beamline. Berlin: Helmholtz-Zentrum für Materialien und Energie GmbH, Suécia: AB Sandvik Coromant, 2017

GENZEL, C. et al. The materials science synchrotron beamline EDDI for energy-dispersive diffraction analysis. **Nuclear Instruments and Methods in Physics Research Section A: Accelerators, Spectrometers, Detectors and Associated Equipment**, v. 578, n. 1, p. 23-33, 2007

GENZEL, C. X-ray stress analysis in presence of gradients and texture. **Advances in X-ray Analysis**, v. 44, p. 247, 2001

GNÄUPEL-HEROLD et al. A model for calculating diffraction elastic constants. **J. Appl. Cryst.** V 45, p. 197-206, 2012

HALVARSSON, M.; TRANCIK, J.; RUPPI, S. The microstructure of CVD κ -Al₂O₃ multilayers separated by thin intermediate TiN or TiC layers. **International Journal of Refractory Metals and Hard Materials**, v. 24, n. 1-2, p. 32-38, 2006

Halvarsson, M.; Langer, T.; Vuorinen, T. Determination of the thermal expansion of κ -Al₂O₃ by high temperature XRD. **Surface and coatings technology** v. 76, 358-362, 1995

HIRSCH, T.; MAYR, P. Residual stresses and residual stress distributions in TiCN- and TiN-coated steels. **Surface and Coatings Technology**, v. 36, n. 3-4, p. 729-741, 1988

IVASHENKO, V.I.; TURCHI, P.E.; SHEVCHENKO, V.I. First-principles study of elastic and stability properties of ZrC–ZrN and ZrC–TiC alloys. **Journal of Physics: condensed matter**, v.21, n.39, p.395503, 2009. DOI: 10.1088/0953-8984/21/39/395503.

KÄLLMAN, I. **Investigation of comb crack generation and wear in milling inserts**. 2014. 46f. Master Thesis - KTH Royal Institute of Technology, School of Industrial Engineering and Management, Stockholm, 2014a

_____. **Internal report TRR 75763**. Suécia: AB Sandvik Coromant, 2014b

KARAGUZEL, U.; BAKKAL, M.; BUDAK, E. Modeling and measurement of cutting temperatures in milling. **Procedia CIRP**, 46, pp.173-176, 2016

KLAUS M.; GENZEL C.; HOLZSCHUH, H. Residual stress depth profiling in complex hard coating systems by X-ray diffraction. **Thin Solid Films**, v. 517, p.1172-1176, 2008

KENNEDY, D.M. et al. Micro shot blasting of machine tools for improving surface finish and reducing cutting forces in manufacturing. **Materials & Design**, v.26, n.3, p.203-208, 2005

KEWEI, X. et al. Thermal effects of residual macrostress and microstrain in plasma-

assisted CVD TiN films. **Surface and Coatings Technology** v. 58, n. 1, p. 37-43, 1993

KIM, J.; SUH, Y. Temperature-and pressure-dependent elastic properties, thermal expansion ratios, and minimum thermal conductivities of ZrC, ZrN, and Zr (C0. 5N0. 5). **Ceramics International**, 43(15), 12968-12974, 2017

KRÖNER, E. Berechnung der elastischen konstanten des vielkristalls aus den konstanten des einkristalls. **Zeitschrift für Physik A Hadrons and Nuclei**, v.151, n.4, p.504-518, 1958

LAGATTA, C. F. **Medições de tensões residuais em filmes finos durante o processo de deposição**. 2011. 82p. Master Thesis - Escola Politécnica, Universidade de São Paulo, São Paulo, 2011

LARSSON, A.; RUPPI, S. Microstructure and properties of CVD γ -Al₂O₃ coatings. **International Journal of Refractory Metals & Hard Materials**, v.19, p.515-522, 2001

LHERMITTE-SEBIRE, I. et al. The adhesion between physically vapour-deposited or chemically vapour-deposited alumina and TiC-coated cemented carbides as characterized by Auger electron spectroscopy and scratch testing. **Thin Solid Films**, v. 138, n. 2, p. 221-233, 1986

MADY, C. E. K. et al. **Cálculo de tensões residuais em filmes finos através de difração de raios-x com ângulo de incidência rasante**. São Paulo: EP/USP, 2008. Available in: http://www.lfs.usp.br/IC/IC2008/apresentacoes/ic2008_apres_carlos.pdf. Accessed in: 20 apr. 2017

MELO, A. C. A. **Estudo das trincas de origem térmica geradas em ferramentas de metal duro durante o fresamento frontal**. 2001. 186f. PhD Thesis - Universidade Federal de Uberlândia, Uberlândia, 2001

MELO, A. C. A. et al. Some observations on wear and damages in cemented carbide tools. **Journal Brazilian Society of Mechanical Sciences and Engineering**, v.28, n.3, p.269-277, 2006

MIRANDA, T. C. **Internal report TRR 75762**. Suécia: AB Sandvik Coromant, 2014

MORENO, M. et al. **Residual Stress Behaviour of Cemented Carbide Coated with CVD Ti(C,N)/a-Al₂O₃ Multilayers: Effect Of Different Blasting Conditions**, In: EuroPM 2019, Proceedings...

MORENO, M. **In-situ stress analyses in CVD multilayers during thermal cycling**. 109p. Final thesis – University of São Paulo, São Carlos School of Engineering, São Carlos, 2017

MURRAY, C. E. Equivalence of Kröner and weighted Voigt-Reuss models for x-ray stress determination. **Journal of Applied Physics**, v. 113, n. 15, p. 153-509, 2013

- MITTERER, C. PVD and CVD hard coatings. In: SARIN, V. K. (Ed.). **Comprehensive hard materials**. New York: Elsevier, 2014. p.449-467
- NOYAN, I.; COHEN, J. X-ray diffraction study of changes in stress-strain distributions during the fatigue of a two-phase alloy. **Materials Science and Engineering**, v. 79 n. 2, p. 149-155, 1986
- NOYAN, I. et al. Residual stress/strain analysis in thin films by X-ray diffraction. **Critical Reviews in Solid State and Material Sciences** v. 20, n. 2, p. 125-177, 1995
- PIERSON, H. O. **Handbook of chemical vapour deposition**. Norwich: Noyes; New York: Willian Andrew, 1999.
- PRAKASH, L. Fundamentals and general applications of hardmetals. In: SARIN, V. K. (Ed.). **Comprehensive hard materials**. New York: Elsevier, 2014. p.29-90.
- PERRY, A. et al. Practical measurement of the residual stress in coatings. **Surface and coatings Technology**, v. 81 n. 1, p. 17-28, 1996
- PERRY, A. et al. X-ray residual stress measurement in TiN, ZrN and HfN films using the Seemann-Bohlin method. **Thin Solid Films**, v. 214, n. 2, p. 169-174, 1992
- PERRY, A.; JAGNER, M. Residual stress in physically vapor deposited films: A study of deviations from elastic behaviour. **Thin Solid Films**, v. 171, n. 1, p. 197-216, 1989
- REBENNE, H.; BHAT, D. Review of CVD TiN coatings for wear-resistant applications: deposition processes, properties and performance. **Surface and Coatings Technology**, v. 63 n.1-2, p. 1-13, 1994
- RIBEIRO, J. E. P. C. **Caracterização experimental e numérica de campos de tensões residuais provocadas por processos de fabrico**. 278f. PhD Thesis – Faculdade de Engenharia, Universidade do Porto, Porto, 2006
- RIEDL, A. et al. Tribological properties of Al₂O₃ hard coatings modified by mechanical blasting and polishing post-treatment. **Wear**, v. 289, p. 9-16, 2012
- RUPPI, S. Deposition, microstructure and properties of texture-controlled CVD α -Al₂O₃ coatings. **International Journal of Refractory Metals and Hard Materials**, v. 23, n. 4-6, p. 306-316, 2005
- RUPPI, S., LARSSON, A.; FLINK, A. Nanoindentation hardness, texture and microstructure of α -Al₂O₃ and κ -Al₂O₃ coatings. **Thin Solid Films**, v. 516, n.18, 5959-5966, 2008
- RUPPI, S.; HALVARSSON, M. TEM investigation of wear mechanisms during metal machining. **Thin Solid Films**, v.353, n.1/2, p.182-188, 1999
- SADIK, M. I. **An introduction to cutting tools materials and applications**. Suécia: AB Sandvik Coromant, 2014

SANCHEZ-BAJO, F.; CUMBRERA, F.L. The Use of the Pseudo-Voigt Function in the Variance Method of X-Ray Line-Broadening Analysis. **Journal of Applied Crystallography**, 30, 427-430, 1997

SCIENCE EDUCATION RESOURCE CENTER, Single-crystal X-ray Diffraction, 2007. Available in:
<http://serc.carleton.edu/research_education/geochemsheets/techniques/SXD.html>. Accessed in: 12. may 2017

SILVA, E. et al. Structure-property relations in ZrCN coatings for tribological applications. **Surface and Coatings Technology**, v.205, n.7, p.2134-2141, 2010

SOUZA, D. C. P. **Estudo da morfologia e estrutura de filmes de oxinitreto de silício (SiOxNy) obtidos pela técnica de PECVD**. 2007. 100p. PhD Thesis - Escola Politécnica, Universidade de São Paulo, São Paulo, 2007

SUTERIO, R. **Medição de tensões residuais por indentação associada à holografia eletrônica**. 2005. 169f. PhD Thesis - Universidade Federal de Santa Catarina, Florianópolis, 2005

SKRZYPEK, S. et al. New approach to stress analysis based on grazing-incidence X-ray diffraction. **Journal of Applied Crystallography**, v. 34, n. 4, p. 427-435, 2001

TAVARES, C. J. **Caracterização estrutural e mecânica de multicamadas de TiN/ZrN depositadas por PVD**. 1997. 125f. Master Thesis - Universidade do Minho, Braga, 199.

TRENT, E.; WRIGHT, P. K. **Metal cutting**. 4thed. Boston: Butterworth-Heinemann, 2000

TKADLETZ, M. et al. Residual stress gradients in α -Al₂O₃ hard coatings determined by pencil-beam X-ray nanodiffraction: The influence of blasting media. **Surface and Coatings Technology**, v. 262, p. 134-140, 2015

TORRES, C. S.; SCHAEFFER, L. Sinterização de WC-Co com atmosfera de argônio, preparado em moinho atritor. In: CONGRESSO BRASILEIRO DE ENGENHARIA E CIÊNCIAS DOS MATERIAIS, 18., 2008, Porto de Galinhas. **Anais...** São Paulo: ABM/ABC/ABPol, 2008

_____. Sinterização do compósito metal duro WC-Co. **Revista Eletrônica de Materiais e Processos**, v.4, n.3, p.58-63, 2009

TRENT, E.; WRIGHT, P. K. **Metal cutting**. 4thed. Boston: Butterworth-Heinemann, 2000

TÖNSHOFF, H. Influence of stress distribution on adhesion strength of sputtered hard coatings. **Thin Solid Films** v. 332, n. 1-2, p. 146-150, 1998

TORRES, C. S.; SCHAEFFER, L. Sinterização de WC-Co com atmosfera de

argônio, preparado em moinho atritor. In: CONGRESSO BRASILEIRO DE ENGENHARIA E CIÊNCIAS DOS MATERIAIS, 18., 2008, Porto de Galinhas. **Anais...** São Paulo: ABM/ABC/ABPol, 2008

_____. Sinterização do compósito metal duro WC-Co. **Revista Eletrônica de Materiais e Processos**, v.4, n.3, p.58-63, 2009

WELZEL, U. et al. Stress analysis of polycrystalline thin films and surface regions by X-ray diffraction. **Journal of Applied Crystallography** v. 38, n. 1, p. 1-29, 2005

WPC TREATMENT: metal surface treatment for motor sports. 2017. Available in: <<http://www.wpctreatment.com/>> Accessed in: 14 may 2017